materials

MDPI

Article

Adsorption and Oxidation of CO on Ceria Nanoparticles Exposing Single-Atom Pd and Ag: A DFT Modelling

Vladimir A. Nasluzov [1], Elena A. Ivanova-Shor [1,*], Aleksey M. Shor [1], Svetlana S. Laletina [1] and Konstantin M. Neyman [2,3]

[1] Institute of Chemistry and Chemical Technology SB RAS, Federal Research Center "Krasnoyarsk Science Center SB RAS", 660036 Krasnoyarsk, Russia; v.nasluzov@yandex.ru (V.A.N.); am.shor@yandex.ru (A.M.S.); shkulepo@rambler.ru (S.S.L.)

[2] Departament de Ciència de Materials i Química Física and Institut de Quimica Teòrica i Computacional, Universitat de Barcelona, 08028 Barcelona, Spain; konstantin.neyman@icrea.cat

[3] ICREA (Institució Catalana de Recerca i Estudis Avançats), 08010 Barcelona, Spain

* Correspondence: eshor1977@gmail.com

Abstract: Various CO_x species formed upon the adsorption and oxidation of CO on palladium and silver single atoms supported on a model ceria nanoparticle (NP) have been studied using density functional calculations. For both metals M, the ceria-supported MCO_x moieties are found to be stabilised in the order MCO < MCO_2 < MCO_3, similar to the trend for CO_x species adsorbed on M-free ceria NP. Nevertheless, the characteristics of the palladium and silver intermediates are different. Very weak CO adsorption and the small exothermicity of the CO to CO_2 transformation are found for O_4Pd site of the $Pd/Ce_{21}O_{42}$ model featuring a square-planar coordination of the Pd^{2+} cation. The removal of one O atom and formation of the O_3Pd site resulted in a notable strengthening of CO adsorption and increased the exothermicity of the CO to CO_2 reaction. For the analogous ceria models with atomic Ag instead of atomic Pd, these two energies became twice as small in magnitude and basically independent of the presence of an O vacancy near the Ag atom. CO_2-species are strongly bound in palladium carboxylate complexes, whereas the CO_2 molecule easily desorbs from oxide-supported $AgCO_2$ moieties. Opposite to metal-free ceria particle, the formation of neither $PdCO_3$ nor $AgCO_3$ carbonate intermediates before CO_2 desorption is predicted. Overall, CO oxidation is concluded to be more favourable at Ag centres atomically dispersed on ceria nanostructures than at the corresponding Pd centres. Calculated vibrational fingerprints of surface CO_x moieties allow us to distinguish between CO adsorption on bare ceria NP (blue frequency shifts) and ceria-supported metal atoms (red frequency shifts). However, discrimination between the CO_2 and CO_3^{2-} species anchored to M-containing and bare ceria particles based solely on vibrational spectroscopy seems problematic. This computational modelling study provides guidance for the knowledge-driven design of more efficient ceria-based single-atom catalysts for the environmentally important CO oxidation reaction.

Keywords: CeO_2-based nanomaterials; density functional calculations; single-atom catalysts; structure; reactivity

Citation: Nasluzov, V.A.; Ivanova-Shor, E.A.; Shor, A.M.; Laletina, S.S.; Neyman, K.M. Adsorption and Oxidation of CO on Ceria Nanoparticles Exposing Single-Atom Pd and Ag: A DFT Modelling. *Materials* **2021**, *14*, 6888. https://doi.org/10.3390/ma14226888

Academic Editors: Simona Bennici and Ilenia Rossetti

Received: 22 October 2021
Accepted: 9 November 2021
Published: 15 November 2021

1. Introduction

Ceria, as a component of catalysts containing transition metals (M) Pd or Ag, is used in numerous applications ranging from the abatement of soot, volatile organic compounds, and CO [1–10] to the production of syngas [11] and CO_2 activation [12,13]. As an active reducible support, ceria facilitates the dispersion of metals and MO_x phases on the surface [7,14–17] and provides lattice O atoms to oxidise reactants [2,9,17–20]. For instance, the interactions within Pd–ceria interfaces allow the synergistic oxidation/reduction of both subsystems [21], promote the oxidation of CO by lattice O atoms, and the oxidation of the reduced ceria by O atoms of CO_2 [22]. Supported transition metals can also enhance

the redox performance and oxygen storage capacity of ceria [23]. Often, high catalytic efficiency is achieved using a nanostructured ceria support via enhanced metal–support interaction, which improves the dispersion of metal particles and suppresses their sintering at elevated temperatures [3,4,7–9,11,19,24–27].

The M-containing surface phases of the aforementioned systems are represented by M_m [6,7,16,24,28,29] and MO_x [6,25,26,30] nanoparticles (NPs), charged metal clusters [7,24,31], solid $M_xCe_{1-x}O_{2-\delta}$ solutions [25–27,32–35], and dispersed M_1 or O_xM_1 ad-species [3,6–9,16,36,37]. Analysis of the crystalline environment of the Pd_1 ad-species revealed that each Pd^{2+} ion in Pd/CeO_2 catalysts prepared by the solution combustion method is coordinated, on average, by three O atoms [34]. This coordination mode of Pd_1 is a feature of adsorption complexes with CO such as O_2Pd_1-$CO/CeO_2(111)$ [8], O_1Pd_1-$CO/CeO_2(111)$ [8], and O_1Pd_1-$CO/CeO_2(100)$ [9], while a Pd_1-$CO/CeO_2(100)$ complex exhibits an O-Pd-O bridge [9]. In many cases, Pd_1 is in a square-planar environment. Pd_1 centres in $Ce_{1-x}Pd_xO_{2-\delta}$ crystals ($x \leq 0.15$) reside on O_4 units adjacent to Ce centres [32]. The doping of ceria with Pd results in a structure with the dopant ion displaced from the initial cationic position to the centre of the O_4 unit [23]. Furthermore, Pd_1 species are attached to the O_4 unit of the $Pd_xCe_{1-x}O_{2-x-\delta}$ lattice incorporating products of water dissociation [27]. Replacing every second upper-layer Ce^{4+} cation and one adjacent to it O^{2-} anion on the $CeO_2(110)$ surface with Pd^{2+} leads to a complex reconstruction and a low-energy surface geometry, with the dopant ion residing close to the centre of the square-planar O_4 site [6]. Stable structures with square-planar O_4Pd are also communicated on Pd-doped $CeO_2(111)$ [33] and edges of ceria NPs at intersecting {111} and {100} nanofacets [35]. Four-fold coordinated Pd adatoms are identified in the most stable O_4Pd structures on the $CeO_2(110)$ surface [20] and {100} nanofacets [37]. The surface O_4 sites are also capable of suppressing the sintering of Ag_1 species, despite the fact that the Ag atom binds to the {100}-O_4 pocket more weakly than other Group VIII–XI metal atoms [37,38]. The aforementioned thermally stable structures are relevant to the development of the single-atom catalysts [36,37,39].

To understand how the role of the ceria support varies in specific catalytic processes, it is crucial to examine the interactions of the involved reactants with various active centres of CeO_2. For the ceria-supported metal catalysts of CO oxidation or CO_2 activation, of primary interest are the interactions of O_2, CO, and CO_2 molecules with the metal–support interfaces [2,8,9,18,20,33,40–43]. Thus, modelling based on density functional theory (DFT) has recently addressed a variety of sites with M_1-O_2, M_1-CO, and M_1-CO_2 entities on ceria [8,9,18,20,40]. The adsorption of CO on a single Pd atom embedded in the defect-free $CeO_2(111)$ surface and that containing O vacancies followed by NO reduction with CO was explored [18,40]. Surface complexes of CO and CO_2 taking part in the catalytic cycle of CO oxidation on $Pd_1/CeO_2(110)$, including Pd_1-CO, Pd_1-CO_2, O_1Pd_1-CO species on the stoichiometric $CeO_2(110)$ surface and Pd_1-CO_2, Pd_1-O_2, O_2-Pd_1-CO ones on the O-deficient $CeO_2(110)$ surface, were calculated [20]. The CO oxidation routes passing via O_1Pd_1-CO, Pd_1-CO, Pd_1-CO_2, O_2Pd_1-CO, and O_1Pd_1-CO_2 moieties on the defect-free $CeO_2(111)$ surface [8] as well as on regular and O-deficient $CeO_2(100)$ surfaces [9] were also quantified. The catalytic CO oxidation according to the Mars-van-Krevelen mechanism combines the elementary steps of oxygen donation from a surface active centre to adsorbed CO and the subsequent replenishment of the support by stream oxygen; the much slower conversions of the first step are found to be rate-determining [8,9,19,20]. In addition to the M_1-CO_2 structures, surface carbonate complexes can be formed on M_1–ceria interfaces before the desorption of CO_2. To this end, the formation of tridentate Pd_1-CO_3 carbonates upon CO_2 adsorption at the interface of Pd_1 and O-deficient $CeO_2(111)$ surface was simulated [13] and the CO vibration frequencies of various ceria-supported Pd-CO species were calculated [8,9]. Unlike the quite extensive computational studies of Pd_1CO_x–ceria systems outlined above, no simulations of analogous Ag_1CO_x–ceria systems have been communicated so far to the best of our knowledge.

Previous studies have developed structural models of low-energy CeO_2 NPs [44–47] and established that their {100} nanofacets notably stabilise single d-metal atoms [38,41,44,48–51]. In this work, we consider monoatomic Pd and Ag species located on a $Ce_{21}O_{42}$ NP [49] as models appropriately describing surface composites formed by single-atom Pd and Ag with nanostructured ceria. These two metals, which are neighbouring in the Periodic Table, interact very differently with ceria and behave as M-based species involved in CO oxidation. The quantification and in-depth understanding of such differences are still missing in the literature.

This study aims to (i) determine the structures of the lowest-energy complexes with CO, CO_2, and CO_3^{2-} moieties resulting from the interaction of CO with Pd and Ag single atoms anchored to the O_4-pocket sites of the stoichiometric and O-deficient ceria NPs, (ii) analyse the structure and properties of these nanostructured adsorption systems versus earlier investigated analogues formed on extended ceria surface containing M_1 centres, (iii) evaluate and rationalise the reactivity differences of Pd_1/NP{100} and Ag_1/NP{100} sites as active centres for CO oxidation (including the effect of M-atom on the formation of CO_3^{2-} prior to CO_2 desorption), and (iv) examine the vibrational fingerprints of the CO_x units accompanying the formation of various surface species. Obtained results related to all these aspects are summarised in the Conclusions section.

2. Models and Details of Calculations

Surface sites of the CeO_2 substrate were represented by a putative global-minimum structure of stoichiometric NP $Ce_{21}O_{42}$ [46,47] exposing four O atoms on its top {100} nanofacet (a so-called O_4-pocket [49]); see Figure 1a. $M_1/Ce_{21}O_{42}$ models were created via anchoring a single M_1 atom (M = Pd or Ag) to the O_4-site of the NP; see Figure 1b,c. The removal of one O atom from the O_4-pocket results in an O-deficient $M_1/Ce_{21}O_{41}$ model with one O vacancy in ceria (not shown in Figures; see Supplementary Material for xyz-structures). CO adsorption does not change the number of O vacancies, whereas the oxidation of CO to CO_2 and further transformation to CO_3^{2-} require the expulsion of one or two O atoms from ceria, generating O vacancies. In the following, the number and origin of O vacancies in the NP $Ce_{21}O_{42}$ are labelled as NP[n/l], where n is a number of O vacancies present prior to CO adsorption (n = 0, 1) and l is a number of O vacancies created by the transfer of O atoms from ceria to the adsorbed CO to form CO_2 or CO_3^{2-} moieties (l = 0, 1, 2). For instance, the stoichiometric and O-deficient NP models $M_1/Ce_{21}O_{42}$ and $M_1/Ce_{21}O_{41}$ are referred to as M/NP[0/0] and M/NP[1/0], respectively.

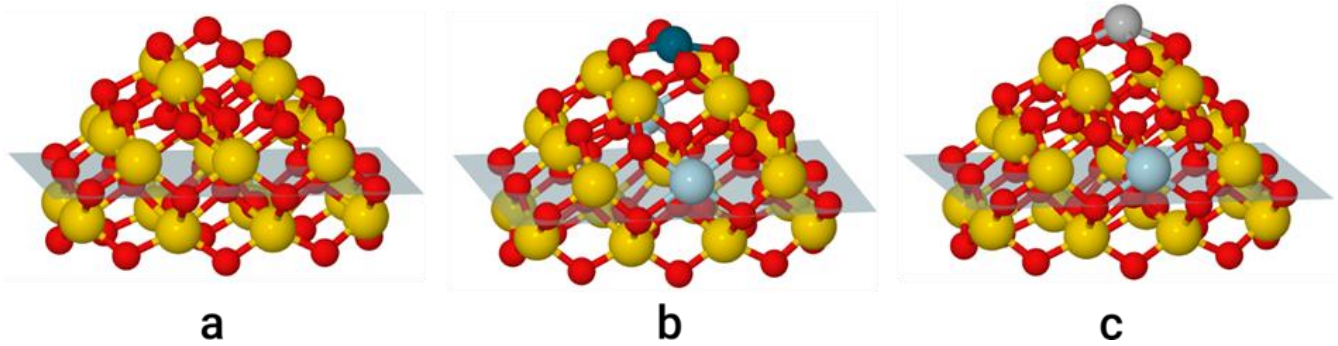

Figure 1. Models of $Ce_{21}O_{42}$ NP: (**a**) without metal atom; (**b**) with Pd atom anchored at {100} facet; (**c**) with Ag atom anchored at {100} facet. The Ce^{4+}, Ce^{3+}, Pd, Ag, and O atoms are shown in yellow, light blue, dark cyan, grey, and red, respectively. The atoms under the transparent plane are omitted for clarity in the Figures 2–4.

The Vienna ab initio simulation package (VASP) [52,53] was employed to determine equilibrium structures of various isomers of the MCO_x/NP[$n/x-1$] complexes formed by the interaction of a CO molecule with Pd/NP[n/0] and Ag/NP[n/0] sites and transition state structures connecting selected equilibrium structures. The plane-wave basis with a 415 eV cutoff for the kinetic energy was used along with the projector-augmented wave

description of the interactions of valence electrons ($2s^2 2p^4$ for O, $4s^1 4d^9$ for Pd, $5s^1 4d^{10}$ for Ag and $5s^2 5p^6 6s^2 5d^1 4f^1$ for Ce) with the atomic cores [54,55]. The NP models were separated by a vacuum space of ~1 nm in the three Cartesian directions (typical cell dimensions $2 \times 2 \times 2$ nm^3) sufficient to eliminate the interaction between periodically repeated NP images [56,57]. All calculations were performed at the Γ-point of the reciprocal space. A generalised-gradient corrected (GGA) exchange-correlated functional PW91 [58] was utilised with the Hubbard-type on-site corrections U [59,60] for Ce4f states providing an improved description of Ce^{3+} ion formation in redox transitions [61,62]. The value of U = 4 eV (PW91 + U = 4 setup) were used in line with previous studies [45,48,61,63,64], though the usage of even such small U values may overestimate the formation energy of carbonates [62,65]. The minimum energy reaction paths MCO/NP[n/0] → MCO_2/NP[n/1] → MCO_3/NP[n/2] were represented with the points of the string method, and the transition states were approximated with polynomial splines [66,67].

Stabilities of the studied systems were quantified based on their formation energies E^f:

$$E^f = E(MCO_x/NP[0/x-1]) - E(CO) - E(M) - E(NP[0/0]) \quad (1)$$

for the MCO_x/NP models obtained from defect-free MCO/$Ce_{21}O_{42}$ structure and

$$E^f = E(MCO_x/NP[1/x-1]) - E(CO) - E(M) - E(NP[0/0]) + 0.5 \times E(O_2) \quad (2)$$

for the MCO_x/NP models obtained from O-deficient MCO/$Ce_{21}O_{41}$ structure, where $E(O_2)$ is total energy of a free O_2 molecule. The binding energies E_b of CO and CO_2 molecules in the models under scrutiny were calculated as follows:

$$E_b(CO) = E(MCO_x/NP[n/x-1]) - E(CO) - E(M/NP[n/0]),\ x = 1\text{–}3;\ n = 0,\ 1 \quad (3)$$

$$E_b(CO_2) = E(MCO_x/NP[n/x-1]) - E(CO_2) - E(M/NP[n/1]),\ x = 2,\ 3;\ n = 0,\ 1 \quad (4)$$

The energies (3) and (4) of the same MCO_2/NP complex were used to estimate the energy of the overall oxidation process CO(gas) + M/NP[n/0] → CO_2(gas) + M/NP[n/1]:

$$E_{ox} = E_b(CO)(MCO_2/NP[n/1]) - E_b(CO_2)(MCO_2/NP[n/1]) \quad (5)$$

or

$$E_{ox} = E_b(CO)(MCO/NP[n/0]) + E^*_{CO2} - E_b(CO_2)(MCO_2/NP[n/1]),\ n = 0,\ 1 \quad (6)$$

where E^*_{CO2} is the energy of CO to CO_2 oxidation at a metal site; i.e., the heat of MCO/NP[n/0] → MCO_2/NP[n/1] transformation:

$$E^*_{CO2} = E(MCO_2/NP[n/1]) - E(MCO/NP[n/0]) \quad (7)$$

where, the asterisk indicates that CO and CO_2 molecules are adsorbed.

Harmonic vibrational frequencies of CO_x groups were calculated by diagonalising the mass-weighted Hessian matrix constructed of differences of the first derivatives of total energy, obtained by displacements by ±0.015 Å in all Cartesian directions of the M, C, and O_x atoms as well as neighbouring ceria atoms within 3.6 Å around them.

3. Results and Discussion

Lowest-energy geometries and formation energies E^f of metal-free CO_x/NP[$n/x-1$] and metal-containing MCO_x/NP[$n/x-1$] complexes are shown in Figures 2–4 (for xyz-structures see Supplementary Material). Table 1 displays the parameters used to specify attachment modes (coordination) of the CO_x groups. Along with the notations MCO_x/NP[$n/x-1$], shorter ones **MxL** and **MxLV** were used for complexes with n = 0 and n = 1, respectively, where **L** is a sequential identifier of the relative energy of a given isomer among isomers with the same **M**, **x**, and **n** (**a**—the most stable, **b**—the second most

stable, **c**—the third most stable). Ce ions with magnetic moments close to 1, at a variance to 0 for most of the cations, were qualified as Ce^{3+} ions resulting from the reduction of Ce^{4+} by electrons of MCO_x moieties or O vacancies.

Table 1. Calculated parameters of the surface complexes shown in Figures 2–4, created by the interaction of CO with the pristine ceria $Ce_{21}O_{42-n}$ and metal–ceria $M/Ce_{21}O_{42-n}$ sites (M = Pd, Ag; n = 0, 1): interatomic distances—r, number of the Ce^{3+} ions—N, difference between the numbers of spin-up and spin-down electrons—m, binding energies of CO—$E_b(CO)$ (Equation (3)) and CO_2–$E_b(CO_2)$ (Equation (4)). Negative energy values correspond to exothermic processes.

System [a]	r(M-C) pm	r(M-O) pm	r(Ce-O) [b] pm	r(C-O) [c] pm	N	m	$E_b(CO)$ eV	$E_b(CO_2)$ eV
Complexes with CO								
Pd1a	296 [d]	-	-	114	2	2	−0.26	-
Pd1b	241	-	-	115	2	2	−0.13	-
Pd1c	188	-	-	116	1	0	0.13	-
Pd1aV	187	-	-	116	4	4	−1.74	-
Ag1a	201	-	-	115	1	1	−0.80	-
Ag1aV	198	-	-	115	3	3	−0.78	-
1a	293 [d]	-	-	114	0	0	−0.26	-
1aV	297 [d]	-	-	114	2	2	−0.23	-
Complexes with CO_2								
Pd2a	206	-	247	2 × 127	2	0	−1.43	−1.20
Pd2b	-	-	314	2 × 118	2	0	−0.41	−0.18
Pd2aV	193	237	268	129; 124	4	4	−2.33	−0.72
Pd2bV	330	-	321	2 × 118	4	4	−1.77	−0.16
Ag2a	356	-	316	2 × 118	3	3	−1.37	−0.16
Ag2b	234	-	268	122; 121	3	1	−1.22	−0.01
Ag2aV	207	-	249	2 × 132	3	1	−1.13	−0.10
Ag2bV	342	-	348	2 × 118	5	1	−1.10	−0.07
2a	-	-	300	2 × 118	2	0	−1.69	−0.25
2aV	-	-	310	2 × 118	4	2	−1.16	−0.15
2bV	-	-	254	2 × 125	3	2	−0.42	0.59
Complexes with CO_3^{2-}								
Pd3a	249	207	260	2 × 133; 125	4	2	−1.68	−1.44
Pd3b	265	209	248	129; 135; 129	3	2	−0.99	−0.75
Pd3c	-	212	245	133; 143; 121	2	0	−0.74	−0.50
Pd3aV	275	211	258	132; 132; 128	4	2	−2.67	−1.06
Pd3bV	288	211	247	131; 143; 122	4	0	−2.28	−0.67
Ag3a	277	221	245	130; 135; 127	3	1	−2.72	−1.49
Ag3b	289	233	247	132; 141; 122	3	1	−2.09	−0.86
Ag3aV	273	216	265	130; 132; 130	5	1	−2.36	−1.40
Ag3bV	291	211	255	129; 146; 122	5	1	−2.09	−1.13
3a	-	-	237	133; 138; 122	2	0	−2.59	−1.15
3b	-	-	250	129; 132; 129	2	2	−2.28	−0.84
3aV	-	-	262	130; 131; 130	4	2	−3.23	−2.22
3bV	-	-	229	133; 137; 122	4	2	−2.53	−1.52

[a] For notations, see Figures 2–4; [b] Average distances of the O of CO_x moiety and nearest neighbour Ce atom; [c] Bond lengths within CO_x moiety; [d] Ce-C contact.

To specify the coordination modes of CO_2 in $MCO_2/NP[n/1]$ and of CO_3^{2-} in $MCO_3/NP[n/2]$ complexes, additional three-digit indices were used [68] resulting in the notation that being invoked only when discussing the coordination modes of CO_x species. For carbonate complexes, a notation abc (integer a, b and c range from 0 to 3) determines numbers of substrate atoms, to which each O atom in CO_3^{2-} is coordinated. The middle digit b corresponds to the O atom with the highest coordination. A dot in indices a.bc or ab.c specifies that two O atoms of CO_3^{2-} (corresponding to a and b or b and c, respectively) form a bidentate bond with one atom of the substrate. Dotless abc identifiers designate CO_3^{2-} groups with each O atom coordinated to a different substrate atom. When the three-digits notation is used to specify coordination of CO_2 in $MCO_2/NP[n/1]$

complexes, the first digit a gives the number of substrate atoms coordinated to C atom. For instance, in Figure 3, each of the atoms of CO_2 in structure 111-**Pd2a** contacts different ions of the $Pd/Ce_{21}O_{41}$ subsystem, and in complex 1.21-**Pd2aV**, one of the O atoms of CO_2 attaches to Pd and Ce atoms of $Pd/Ce_{21}O_{40}$, and C atom also to Pd.

3.1. Structure, Charge State, and Relative Energies of Surface Complexes with CO_x

3.1.1. Adsorption Sites

The particle $Ce_{21}O_{42}$ exposes a {100} nanofacet (Figure 1a), which can bind metal atoms much stronger than its {111} nanofacets do [38]. We anchored single Pd and Ag atoms to the {100} nanofacet composed of four nearly coplanar two-coordinated oxygen centres forming an O_4-pocket with diagonals of 459 and 443 pm. This arrangement is appropriate for accommodating transition metal cations with typical M-O bond lengths of 185–210 pm [37]. The distances between the O_4-pocket atoms and the neighboring Ce atoms, 214–215 pm, are shortened versus the Ce-O distances of three-coordinated surface O atoms and four-coordinated inner O atoms, 230–250 pm.

The Ag atom binds by 2.27 eV to the O_4-site (Figure 1b), making the two diagonals of the latter almost equal. The two types of Ag-O bond lengths, 236 and 242 pm, agree with Ag-O distances of 239 and 241 pm calculated at the same theory level on a larger $Ce_{40}O_{80}$ NP [37]. Furthermore, the present location of the Ag atom 96 pm above the O_4-plane is close to the elevation by 90 pm on $Ce_{40}O_{80}$ [37]. A slightly larger above-plane elevation, by 102 pm, was calculated for a two-fold coordinated Ag single atom adsorbed on the $Fe_3O_4(001)$ surface with energy 2.75 eV [69]. Ag atom adsorption moves O_4 centres upwards, elongating the involved Ce-O distances to 218–223 pm. One Ce ion reduced to +3 state, pointing to the Ag^+ oxidation state.

The Pd adatom is located nearly in the O_4 plane (Figure 1c), with an out-of-plane displacement of 18 pm, adopting a favourable planar coordination. All four Pd-O bonds are equal to 205 pm—exactly the same as for the $Pd/Ce_{40}O_{80}$ model [37]. The formation of PdO_4 species moves O atoms closer to Pd, contracting diagonals of the O_4 square to 408 pm and elongating the corresponding Ce-O distances to 230 pm—the value typical for three-coordinated O centres. The high adsorption energy of the Pd atom, 4.24 eV, further increases upon interactions with the O_4-site of larger ceria NPs [37]. Two Ce^{3+} ions appeared upon Pd adsorption, indicating the oxidation state Pd^{2+}.

An O-deficient site is created by the removal of the weakest bonded O atom (with $E(O_V)$ = 1.87 eV, Table 2) from the O_4-pocket of the $Ce_{21}O_{42}$ particle (Figure 1). Two Ce^{3+} centres resulting from the O removal in the second Ce layer cause the elongation of the Ce^{3+}-O bonds by ~0.1 Å. O vacancy formation in the $Ag/Ce_{21}O_{42}$ model requires 2.08 eV (Table 2), nearly the same amount as for the metal-free O_4-site. Thus, an extra energy cost due to breaking the Ag-O bond (in addition to two Ce-O bonds of $Ce_{21}O_{42}$) is estimated at ~0.2 eV. Two Ag-O bonds are contracted to 2.15 Å upon O removal, whereas the third bond is elongated from 2.36 to 2.49 Å. A similar bonding situation has been found in our previous work, where an Ag single atom was anchored to the bottom {100} nanofacet of $Ce_{21}O_{42}$ NP [38]. Alternatively, the creation of an O-deficient $Pd/Ce_{21}O_{41}$ site requires substantial energy costs of 3.08 eV (Table 2).

Table 2. Reaction and activation energies ($E^{\neq}$) on the pristine ceria $Ce_{21}O_{42-n}$ and metal–ceria $M/Ce_{21}O_{42-n}$ models (M = Pd, Ag; n = 0, 1) depicted in Figures 2–4. Oxygen vacancy formation energies $E(O_V)$ are also shown. Negative energy values correspond to exothermic processes. All energies are in eV.

Model [a]		$CO \rightarrow CO_2$			$CO_2 \rightarrow CO_3$	
	$E(O_V)$	E_{ox} [b]	E^*_{CO2} [c]	$E^{\neq}$	E^*_{CO3} [d]	$E^{\neq}$
$Ce_{21}O_{42}$	1.87	−1.44	−1.43	1.02	−0.90	0.27
$Ce_{21}O_{41}$	2.31	−1.01	−0.92	0.82	−2.07	0.82
$Ag/Ce_{21}O_{42}$	2.08	−1.21	−0.52	0.88	−1.50	0.78
$Ag/Ce_{21}O_{41}$	2.28	−1.03	−0.35	0.53	−1.23	1.73
$Pd/Ce_{21}O_{42}$	3.08	−0.23	−1.30	0.51	−0.25	1.83
$Pd/Ce_{21}O_{41}$	1.70	−1.61	−0.59	1.06	−0.34	1.80

[a] System on which initial CO adsorption takes place; [b] reaction energy of the CO oxidation CO(gas) + NP[n/0] → CO_2(gas) + NP[n/1] or CO(gas) + M/NP[n/0] → CO_2(gas) + M/NP[n/1]; [c] reaction energy of the CO_2 formation CO/NP[n/0] → CO_2/NP[n/1] or MCO/NP[n/0] → MCO_2/NP[n/1]; [d] reaction energy of CO_2/NP[n/1] → CO_3/NP[n/2] or MCO_2/NP[n/1] → MCO_3/NP[n/2] conversion.

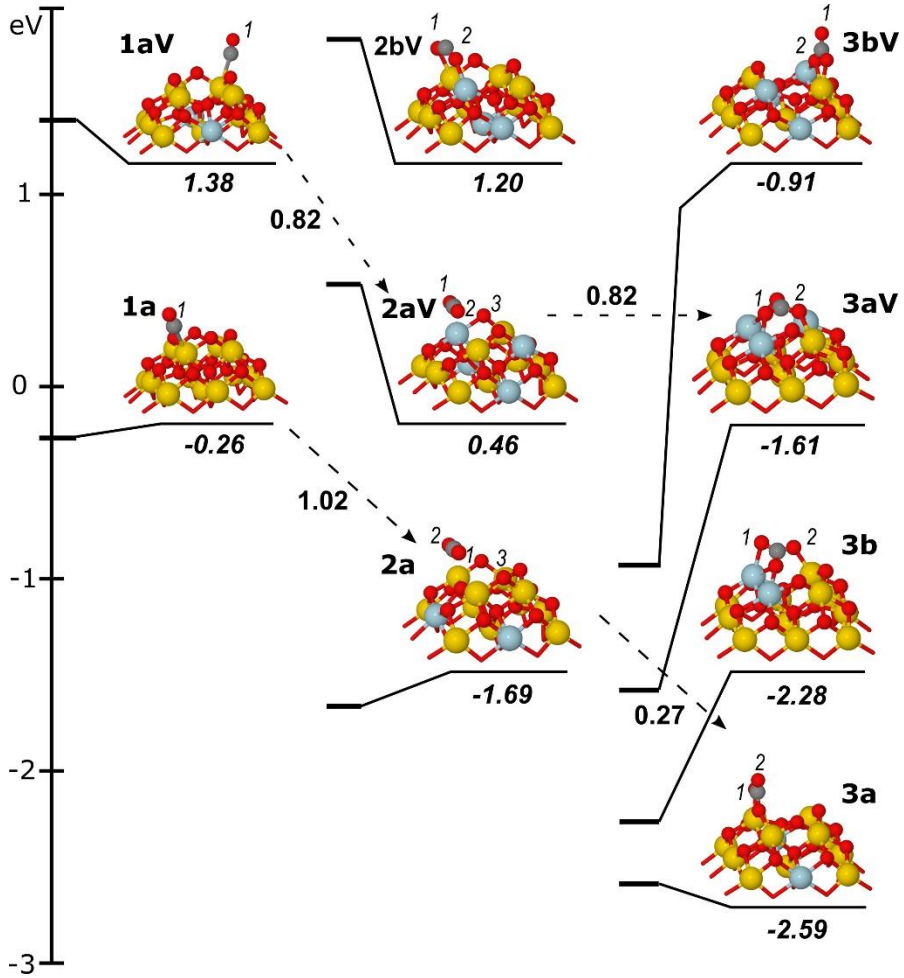

Figure 2. Structures and formation energies E^f (in eV) of the complexes created by the interaction of CO with the $Ce_{21}O_{42-n}$ sites (n = 0, 1): $CO/Ce_{21}O_{42}$ (**1a**), $CO/Ce_{21}O_{41}$ (**1aV**), $CO_2/Ce_{21}O_{41}$ (**2a**), $CO_2/Ce_{21}O_{40}$ (**2aV, 2bV**), $CO_3/Ce_{21}O_{40}$ (**3a, 3b**) and $CO_3/Ce_{21}O_{39}$ (**3aV, 3bV**). Activation energies ($E^{\neq}$) of selected transition states are shown near the dashed arrows connecting corresponding initial reagent and product. The C atoms are shown in dark grey. O atoms numbered with "1", "2", and "3" enter CO, CO_2, and CO_3 moieties, respectively. For further explanations, refer to the main text and the Figure 1 caption.

Evidently, an extra energy of ~1.2 eV is needed to cleave one Pd-O bond. Note that the Pd atom remains after O removal in a virtual square-planar environment with one coordination site empty and the lengths of the remaining three Pd-O bonds unchanged, 206–209 pm, vs. the PdO_4 site of $Pd/Ce_{21}O_{42}$. No reduction of Ag^+ and Pd^{2+} ions occurs upon O vacancy creation, since the leaving O atom donates two electrons to two Ce^{4+} ions, increasing the number of Ce^{3+} centres by two (to three for Ag/NP and to four for Pd/NP).

3.1.2. Carbonyl Species

Let us first consider the adsorption of a CO molecule on a Ce ion of bare ceria particles (Figure 2). For both the pristine and O-deficient structures, CO adsorption energy is very small, at −0.26 and −0.23 eV, respectively (Table 1). No geometry changes are calculated upon bringing together the CO molecule and ceria species. In particular, the C-O bond is retained at 114 pm as in the free CO molecule. The C end of the CO adsorbate is 293 (**1a**) and 297 pm (**1aV**) away from the nearest Ce^{4+} ion of NP (Table 1). CO forms angles at 176° and 172° with the Ce site. Thus, CO is rather physisorbed than chemisorbed on the Ce site of the pristine and reduced forms of the metal-free NP. The same geometry and adsorption energy of −0.26 eV (Table 1) was calculated for the Pd-containing **Pd1a** structure with the CO molecule bound to a Ce^{4+} ion (Figure 3), indicating that the filling of the O_4-pocket by the Pd atom mainly affects the local structure of the PdO_4 site.

An even smaller CO adsorption energy, −0.13 eV, was calculated for the coordinatively saturated Pd centre of the PdO_4 site of the unreduced model (**Pd1b**, Figure 3). Here, CO binds the Pd atom at an angle of 131° and rather long Pd–C contact of 241 pm.

CO adsorption causes minor distortions in the $Pd/Ce_{21}O_{42}$ structure: Pd-O bonds extend from 205 to 207 pm, and Pd moves by 27 pm above the O_4 plane. The C-O bond elongates by just 1 pm vs. gas-phase CO. No CO adsorption was reported on Pd atoms in the PdO_4 environment saturated by two O centres of the CeO_2{100} surface and two O adatoms [9]. Furthermore, $E_b(CO) < -0.2$ eV was calculated for coordinatively saturated Pd atoms in PdO(100). Thus, a very low $E_b(CO)$ for **Pd1b** is related to the saturation of the coordination sphere of the Pd atom in the O_4-pocket of the {100} nanofacet by O atoms; the formation of an additional Pd-C bond competes with quite strong Pd-O bonds. The exceptional stability of Pd^{2+} ions in square-planar oxygen environment in CeO_2 materials is also claimed in other experiments [6,27,32]. Note that CO adsorption on all Pd-containing models does not change the oxidation state Pd^{2+}, except for **Pd1c** with an endothermic mode by 0.13 eV CO adsorption (Table 1), where a $Ce^{3+} \rightarrow Ce^{4+}$ transition indicated a reduction to Pd^+.

In an O-deficient structure, **Pd1aV** (Figure 3), the adsorbed CO occupies one of four places around Pd. This results in Pd-C bond shortening to 187 pm (Table 1), as in Pd_1-CO/CeO_2(110) complexes bonded with two (Pd-C = 184 pm) and three O surface atoms (Pd-C = 188 pm) [20]. The Pd-C-O angle in **Pd1aV** is close to 180°. The elongation of the C-O distance from 114 to 116 pm indicates noticeable d → 2π* back-donation. In **Pd1aV**, CO binds at a vacant coordination site around Pd, no bonds are broken, and adsorption induced geometry changes are minor. As a result, $PdCO/Ce_{21}O_{41}$ is stabilised by 1.7 eV with respect to separated $Pd/Ce_{21}O_{41}$ and CO fragments (Table 1). Interestingly, similarly strong CO binding as that for **Pd1aV**, 1.77 eV, and a Pd-C distance of 186 pm were calculated for the two-fold coordinated single Pd atom in Pd_1/Fe_3O_4(001) [69]. The CO bond to the isolated Pd atom is also similarly strong, at 1.8 eV [70]. The values of 1.6 eV [8] and 1.9 eV [9] were calculated for Pd_1-CO/CeO_2(111) and O_1Pd_1-CO/CeO_2(100) complexes, respectively, with Pd_1 coordinated to three O atoms including that of isolated O_1Pd_1 species. A CO adsorption energy of −1.5 eV was calculated for the Pd_1-CO/CeO_2(110) complex with the Pd^+ ion between two three-fold O atoms [20]. In the series of complexes Pd_1-CO/CeO_2(111), O_1Pd_1-CO/CeO_2(111), and O_2Pd_1-CO/CeO_2(111), $E_b(CO)$ decreases (by module) with the growth of the Pd_1 coordination number from 1.6 to 0.9 and to 0.6 eV [8].

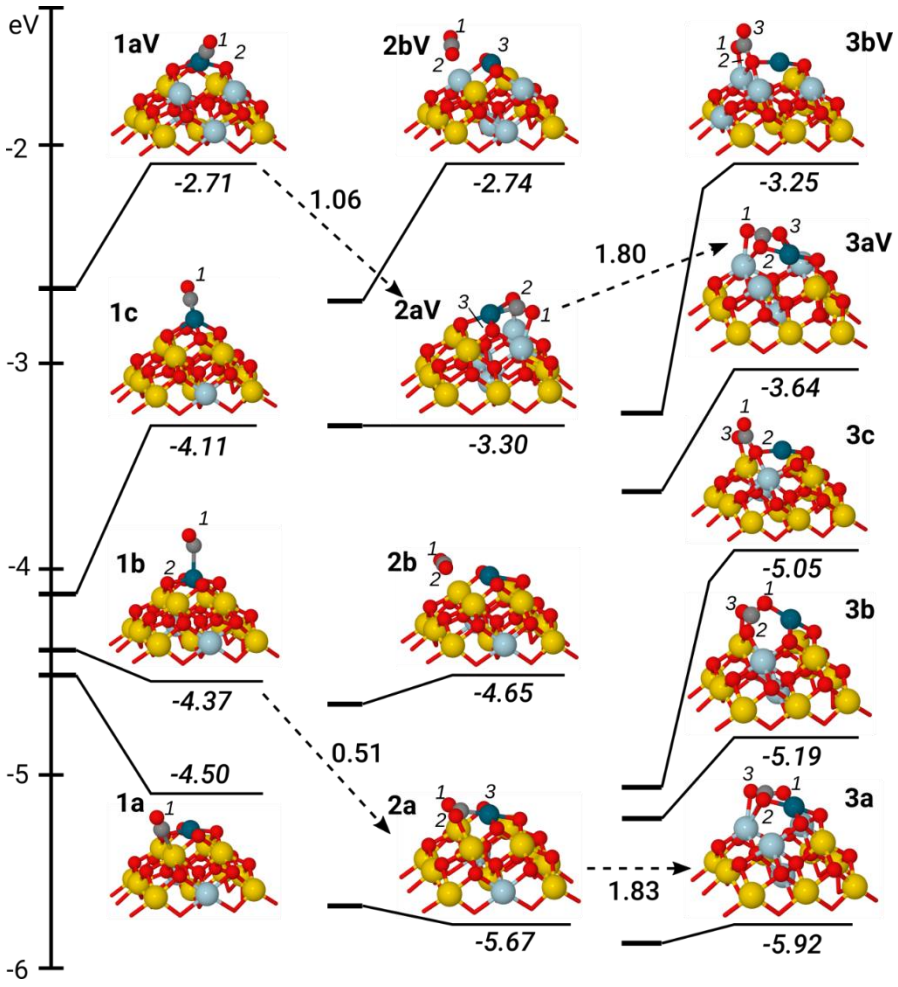

Figure 3. Structures and formation energies E^f (in eV) of the complexes created by the interaction of CO with the $PdCe_{21}O_{42-n}$ sites (n = 0, 1): $PdCO/Ce_{21}O_{42}$ (**Pd1a, Pd1b, Pd1c**), $PdCO/Ce_{21}O_{41}$ (**Pd1aV**), $PdCO_2/Ce_{21}O_{41}$ (**Pd2a, Pd2b**), $PdCO_2/Ce_{21}O_{40}$ (**Pd2aV, Pd2bV**), $PdCO_3/Ce_{21}O_{40}$ (**Pd3a, Pd3b, Pd3c**) and $PdCO_3/Ce_{21}O_{39}$ (**Pd3aV, Pd3bV**). Activation energies ($E^{\neq}$) of selected transition states are shown near the dashed arrows connecting corresponding initial reagent and product. For further explanations, refer to the main text and the captions to Figures 1 and 2.

The binding of CO to O-defect-free **Ag1a** and O-deficient **Ag1aV** complexes is moderately strong, at about 0.8 eV (Table 1), and essentially independent of the coordination—AgO_4 or AgO_3—of the Ag atom. This adsorption energy value fits the calculated values of −0.85 eV for CO adsorption at the two-fold coordinated Ag single atom in the $Ag_1/Fe_3O_4(001)$ site and −0.94 eV for the two-fold coordinated Ag atom at the $AgO_2(111)$ surface well [69]. Structures of the AgCO fragments in **Ag1a** and **Ag1aV** are very similar (Figure 4). The Ag-C distance of ~200 pm (Table 1) coincides with the value computed for the Ag_1CO moiety at $Fe_3O_4(001)$. The C-O bond, 115 pm, is 1 pm longer than that in the free CO molecule. The Ag-C-O angle of ~170° points to slight deviation from the typically favoured linear bonding geometry. In both structures, CO adsorption triggers a further displacement of Ag atom out-of-plane of neighbouring O atoms, reaching values of 132 and 152 pm for **Ag1a** and **Ag1aV**, respectively (vs. 96 and 60 pm for CO-free structures). Ag-O bond lengths vary substantially, ranging from 237 to 258 pm for the AgO_4 unit and from 224 to 264 pm for the AgO_3 unit. The notable distortions at the Ag/CeO_2 interface are not reflected in CO adsorption energies. This finding is in line with the quite weak Ag-O bonding estimated at 0.2 eV (see Section 3.1.1).

In summary, the modification of the ceria NP with single Pd and Ag atoms strongly affects its affinity to CO. Effects of Pd and Ag atoms are different. Due to strong Pd-O

bonds, the saturated PdO_4 site is almost inactive towards CO adsorption, whereas the PdO_3 unit with a vacant coordination place readily traps CO with a substantial energy gain. In contrast, AgO_4 and AgO_3 centres with weak Ag-O bonds and a more flexible geometry are more prone to adsorb CO molecules with equally moderate energies.

3.1.3. Carbon Dioxide Species

For the metal-free ceria, only weakly adsorbed CO_2 species were calculated: binding energies are −0.25 and −0.15 eV for **2a** and **2aV** models, respectively (Table 1). These energies are comparable with the values calculated for linearly-adsorbed CO_2 at extended CeO_2(100), (110), and (111) surfaces [71–76]. In both complexes, the linear geometry of CO_2 as in the gas-phase molecule is preserved: C-O bond lengths are 118 pm and the O-C-O angle is 178°. The C atoms of CO_2 molecules are located above the O vacancy parallel to the surface of NP (Figure 2); in case of **2a**, the O atom from the low-lying layer moves up and forms an O-C contact of 288 pm (vs. 390 pm in **2aV**).

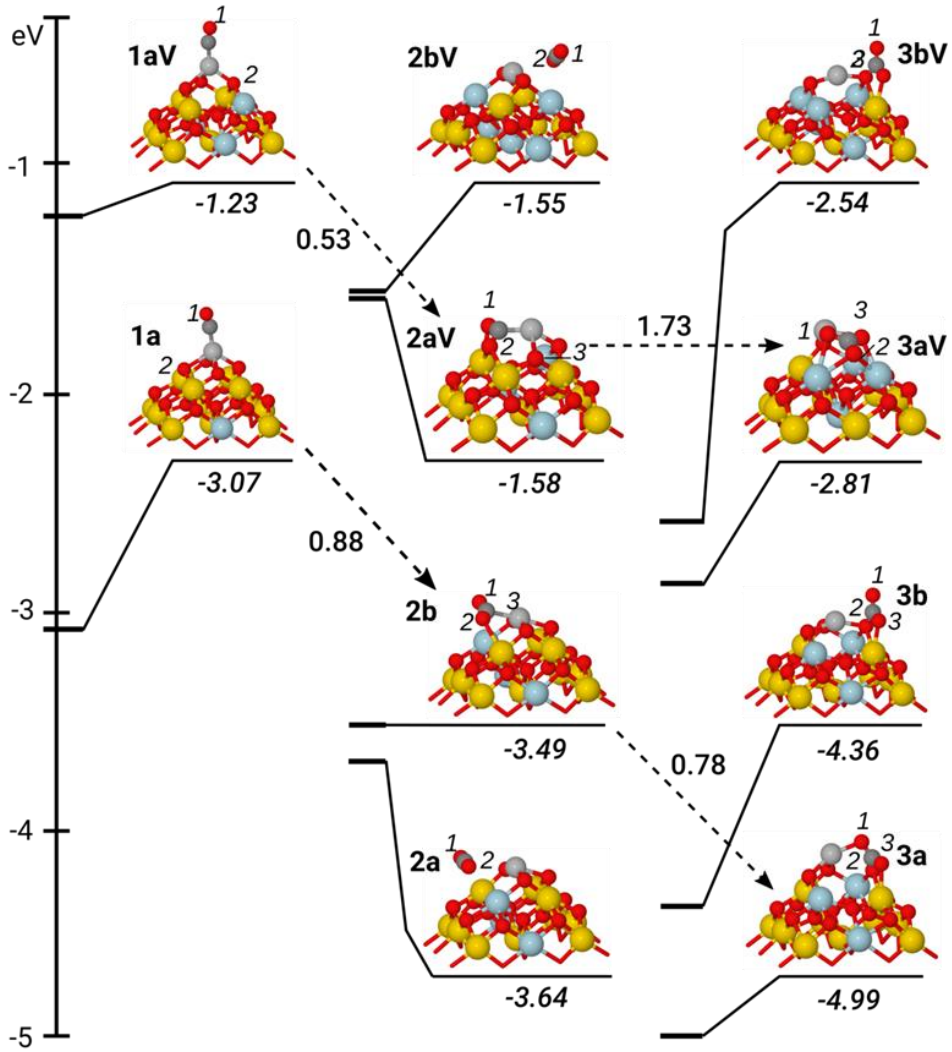

Figure 4. Structures and formation energies E^f (in eV) of the complexes created by the interaction of CO with the $Ag/Ce_{21}O_{42-n}$ sites (n = 0, 1): $AgCO/Ce_{21}O_{42}$ (**Ag1a**), $AgCO/Ce_{21}O_{41}$ (**Ag1aV**), $AgCO_2/Ce_{21}O_{41}$ (**Ag2a, Ag2b**), $AgCO_2/Ce_{21}O_{40}$ (**Ag2aV, 2bV**), $AgCO_3/Ce_{21}O_{40}$ (**Ag3a, Ag3b**) and $AgCO_3/Ce_{21}O_{39}$ (**Ag3aV, Ag3bV**). Activation energies ($E^{\neq}$) of selected transition states are shown near the dashed arrows connecting corresponding initial reagent and product. For further explanations, refer to the main text and the captions to Figures 1 and 2.

The contacts of O atoms of the CO_2 group with Ce atoms are ~300 pm in **2a** and 304–331 pm in **2aV** (Table 1). All attempts to locate more stable structures with a bent CO_2 moiety have led to carbonate moieties (described in detail in Section 3.1.4). No minima corresponding to bent CO_2 structures of carboxylate type were found. The only located structure with distorted CO_2 (**2bV** at Figure 2) was found to be 0.75 eV less stable relative to the linear **2aV** model. It features C-O bond lengths of 125 pm and an O-C-O angle of 131°. The O atoms of CO_2 are at 252 and 257 pm from Ce atoms. The positive CO_2 binding energy in **2bV** of 0.6 eV (Table 1) indicates exothermic CO_2 release. Since only one Ce^{3+} ion is present after CO to CO_2 transformation, CO_2 in **2bV** is negatively charged, forming a CO_2^- anion. Thus, CO_2 binds weakly and easily desorbs from bare $Ce_{21}O_{42-x}$ NP.

The metal-containing Pd/NP and Ag/NP models also feature structures with "linear" and "bent" CO_2 (Figures 3 and 4). Similar to the bare ceria, linear CO_2 is weakly bound in **Pd2b**, **Pd2bV**, **Ag2a,** and **Ag2bV**, by less than 0.2 eV (Table 1). All distances between atoms of CO_2 molecule and ceria are longer than 300 pm. In contrast, in "bent" CO_2 structures **Pd2a**, **Pd2aV**, **Ag2b,** and **Ag2aV,** CO_2 approaches more closely to the NP surface and forms C-M and O-Ce bonds at 193–234 and 250–270 pm, respectively. Interestingly, despite the sizable changes at the metal–adsorbate interface when going from "linear" to "bent" structures, the pairs **Ag2aV**/**Ag2bV** and **Ag2a**/**Ag2b** are isoenergetic within 0.15 eV. This observation supports our earlier finding that the formation of a new Ag-ligand bond (e.g., Ag-C with CO_2) does not require substantial energy (limited to 0.2 eV). The bonds of CO_2 in **Ag2b** are symmetrically stretched to 121 pm and the O-C-O angle is reduced to 145°, thus indicating the formation of a weakly-bound carboxylate-like complex. CO_2 is coordinated to Ag via the C atom at a distance of 234 pm and forms an (O)C-Ag-O angle of 175° with the Ag-O bond in trans-position. The Ag atom in $AgCO_2/Ce_{21}O_{41}$ rises above the O_3-plane by 52 pm (vs. 132 pm in $AgCO/Ce_{21}O_{42}$), similar to O-deficient adsorbate-free $Ag/Ce_{21}O_{41}$ complex (60 pm). Thus, the surrounding of the Ag center in **Ag2b** is nearly square-planar. The formation of the CO_2 moiety in **Ag2aV** does not lead to the entire detachment of the surface O* atom by adsorbed CO (Figure 4). Rather, the **Ag2aV** model can be viewed as a complex with CO inserted into the O*-Ag bond; as a result, the O*-Ag distance is stretched from 227 to 287 pm. Upon this insertion, Ce-O* bonds of the Ce-O*-Ce bridge are elongated from 218–233 pm in **Ag1aV** to 249–257 pm in **Ag2aV** (Table 1). The shortest Ce-O* distance in **Ag2b** is 268 pm. The CO_2 fragment in **Ag2aV** is more strongly distorted than in **Ag2b**: C-O bonds are 130 pm and the O-C-O angle is quite small, at 114°. The Ag-CO_2 distance (207 pm) is typical for metal–CO_2 complexes with an η^1-C type of CO_2 coordination [77]. Energies of **Ag2b** and **Ag2aV** models differ by 1.9 eV, the value close to the O vacancy formation energy at the O_4-pocket (Table 2).

The $PdCO_2$-containing complexes, **Pd2a** and **Pd2aV**, with a "bent" CO_2 moiety (Figure 3) are characterised by substantial CO_2 binding energies of −1.2 and −0.7 eV, respectively (Table 1). Both models exhibit a carboxylate-like structure of CO_2: C-O bonds are 124–130 pm long and the O-C-O angle is 130 ± 3°. In the **Pd2a** structure, CO_2 is η^1-coordinated to the Pd atom with the Pd-C distance, 206 pm, comparable to three Pd-O bonds around the metal center, 208–220 pm. In the **Pd2aV** complex, the CO_2 molecule is η^2-coordinated to Pd via the short Pd-C bond, 193 pm, and long Pd-O contact of 237 pm; two other Pd-O bond lengths are 205–220 pm. The Pd atom in both **Pd2a** and **Pd2aV** complexes is nearly in a square-planar environment with Pd shifting from the ligand plane by 25–30 pm. Interestingly, no ceria-supported PdO_3 structures with calculated CO_2 binding energies more than −0.4 eV (by module) were found in the literature [8,9,20]. The larger values −0.82 eV [20] and −0.96 eV [8] were calculated for PdO_2 units at CeO_2(110) and CeO_2(111) surfaces. In part, this can be explained by a favourable square-planar geometry within the O_3Pd-CO_2 fragment formed at the {100} nanofacet of $Ce_{21}O_{42}$ NP. Indeed, such structures are hindered at extended CeO_2 surfaces by geometrical constrains.

Thus, similar to the CO case, the strongest bonding is calculated for the PdO_3 site with one vacant coordination place. This is followed by the PdO_2 unit with two vacant valences, which binds CO_2 in a side-on fashion. Both structures are characterised by CO_2 bending.

The adsorption of CO_2 in linear mode results in an energy gain less than 0.2 eV for both Pd and Ag derivatives. In contrast to the Pd derivatives, both "linear" and "bent" modes have similar small adsorption energies for the Ag systems. Thus, AgO_3 and AgO_2 sites again do not show differences in adsorption properties, whereas their Pd analogs do.

3.1.4. Carbonate Species

Carbonate species are formed upon the coordination of the CO_2 molecule via the C atom to an O center of ceria NP. Thus, CO_3^{2-} formation can be considered as a form of CO_2 adsorption, and CO_2 binding energy can be applied to the estimation of the stability of these carbonate species.

The carbonate-like CO_2 adsorption at bare ceria NPs with binding energies of 0.84–2.22 eV (Table 1) is the most exothermic of all types of CO_2 coordination discussed above. The strongest binding of 2.22 eV is calculated for the tridentate 2.2.2-structure (**3aV**, Figure 2), with each O atom of the CO_3 moiety coordinated to two Ce ions. The flat-lying carbonate fragment of **3aV** fills two O vacancies with its oxygen atoms; i.e., all O atoms of the CO_3 moiety are in neighbouring O-positions of the O_4-pocket. The $E_b(CO_2)$ energy for **3aV** is between –1.9 and –2.3 eV, respectively, calculated for its formal 2.2.2-CO_3 analog on regular CeO_2(100) [78] and bidentate 220-CO_3 on O-deficient CeO_2(110) [74]. The 2.2.2-model features three C-O bonds equally stretched to 130 pm and O-C-O angles of 118 ± 2°. Three of four Ce^{3+} ions are located in the Ce_4 square just below the O_4-pocket of the {100} nanofacet. The other tridentate 1.21-structure **3b** is stabilised by only 0.84 eV relative to the sum CO_2 + NP (Table 1). Here, each of the two O atoms of CO_2 has only one contact with Ce ions of 238 and 247 pm. As in the **3aV** model, the CO_3 fragment in **3b** has a slightly distorted C_{3V} symmetry, with C-O bonds of 130 ± 2 pm and O-C-O angles of 117–122°. Its CO_3 plane is tilted by 40° relative to the Ce_4 layer. The CO_2 binding energy in the 1.21-carbonate is comparable to value −0.72 eV calculated for the flat-lying 2.21-CO_3 structure [71] formed upon CO adsorption at the stoichiometric CeO_2(100) surface with every second atom of the O layer removed. The deletion of an O atom from 1.21-**3b** to give 2.2.2-**3aV** costs only 0.67 eV. Thus, energy for the removal of a lattice O atom (~2.3 eV for formation of a 2nd O vacancy) is compensated by the formation of two new O-Ce contacts in **3aV** with ~1.6 eV energy gain. At variance, the energy difference between two 1.20-structures **3a** → **3bV**, with a bidentate coordination, 1.68 eV, does not decrease with respect to $E(O_v)$ for $Ce_{21}O_{42}$ → $Ce_{21}O_{41}$ transition, since both models have a similar bonding pattern of carbonate species. Thus, not surprisingly, the CO_2 binding energies for **3a** and **3bV** models are not very different, at –1.15 and −1.52 eV, respectively (Table 1). In both **3a** and **3bV** models, the CO_3 moiety is tied by three O-Ce bonds at 227, 238, and 245 pm. The three O-C bond lengths are different and increase from 122 to 133 and to 137 pm with the growing coordination number of O atom from 0 to 1 and to 2, respectively. Notably, at the O-deficient ceria, the flat-lying structure **3aV** is preferred over the standing one **3bV** by 0.7 eV. A similar difference of 0.84 eV was calculated for CO_3 moieties oriented parallel and perpendicular to the O-defective CeO_2 (100) facet [71]. The trend of destabilising carbonate species at ceria substrates upon surface enrichment by O atoms [71] is also supported by the present data.

Three types of carbonate structures—standing (perpendicular), tilted and flat-lying (parallel)—were also located for metal-containing ceria NPs (Figures 3 and 4). The "standing"-type carbonate species is coordinated in a bidentate way in 1.30-models **Pd3c**, **Pd3bV**, **Ag3b**, and **Ag3bV**. These structures are very similar to 1.20-carbonates **3a** and **3bV** at bare ceria NPs, with the difference that the CO_3 moiety is additionally bound with the M center via one short M-O bond of 211 pm (233 pm in **Ag3b**). This extra metal–oxygen bond induces the elongation of other three O-Ce contacts by 5–15 pm as well as elongates O···CO_2 contact by 4–9 pm, which probably weakens CO_2 binding from −1.15–1.52 eV in metal-free models to −0.86–1.13 and −0.39–0.50 eV in Ag- and Pd-carbonates, respectively (Table 1). Thus, for Pd-systems, carbonate-like CO_2 adsorption in a "standing" mode is

weaker than adsorption in carboxylate $PdCO_2$ form. Notably, Pd is in a zero-oxidation state in both types of complexes.

Stronger CO_2 bindings, of −1.44 and −1.40 eV, were calculated for the "flat-lying" structures 2.2.1-**Pd3a** and 2.2.2.-**Ag3aV**, respectively (Table 1). The CO_3 fragment is bidentately coordinated with two M-O contacts: almost equal in **Pd3a** (207 and 211 pm) and asymmetric in **Ag3aV** (216 and 265 pm). In the **Pd3a** structure, all O atoms of the CO_3 moiety leave their lattice positions to form short Pd-O bonds (Figure 3). This leads to the creation of a CO_3^{2-} unit with a formal charge of −2 and oxidation of Pd to the +2 oxidation state. Even shorter M-O bonds are formed between metal centres and O atoms of the ceria support: 201–202 pm for Pd-O and 206 pm for Ag-O bonds. Thus, the Pd atom is four-coordinated whereas Ag is three-coordinated by O ligands. Importantly, the PdO_4 unit in **Pd3a** is in a slightly distorted stable square-planar configuration. Likely, this contributes greatly to making **Pd3a** the most energetically favourable among all studied ceria-supported $PdCO_x$ species. The **Pd3a** complex is even 0.25 eV more stable than another square-planar structure: carboxylate **Pd2a** complex with O_3PdCO_2 unit. The plane of the CO_3 subsystem forms a small angle of about 20° with the O_3M plane. The "lying" **Ag3aV** structure is only 0.27 eV stabilised with respect to "standing" **Ag3bV,** whereas the analogous stabilisation for **Pd3a** → **Pd3c** transition reaches 0.87 eV.

The **Ag3a** 1.21-complex with the "tilted" coordination mode of CO_3 is the most favourable Ag-carbonate structure with a CO_2 adsorption energy of −1.49 eV (Table 1). Similar to the 1.30-model **Ag3b**, the CO_2 moiety in the **Ag3a** structure is tied in an η-C,O fashion with ceria support by means of two bonds. While the distance O-C-O···Ce is the same in **Ag3a** and **Ag3b**, the O···CO_2 contact in **Ag3a** is shortened to 135 pm from 141–146 pm in **Ag3b**. The shorter Ag-O contact of 221 pm (vs. 233 pm in **Ag3b**) is formed with the O atom, which has no bonds with CeO_2; this is comparable to the Ag-O bond length of 218 pm with ceria. Remarkably, "tilted" 1.21-complex **Ag3a** is by 0.63 eV stabilised with respect to "standing" 1.30-model **Ag3b** with an $E(CO_2)$ of −0.86 eV and reaches a CO_2 adsorption energy of −1.52 eV of the metal-free "standing" **3bV** model. 1.21-**Ag3a** complex has a nearly identical CO_2 adsorption energy (within 0.1 eV) to the "lying" 2.2.2-**Ag3aV** model. In both complexes, the cationic Ag^+ center is three-coordinated. Despite the closer contact of the CO_3 unit with ceria support in the 2.2.2-model, its formation from the **Ag3a** structure by the removal of O bound to the Ag atom requires a substantial energy of 2.18 eV. In contrast, O deletion from 1.21-**Pd3b** to give 2.2.1-**Pd3aV** is endothermic by only 1.55 eV. Both "tilted" complexes, **Pd3b** and **Pd3aV**, have CO_2 adsorption energies of −0.75 and −1.06 eV, respectively, bracketing the value for the "tilted" metal-free **3b** complex. Note that the **Pd3b** → **Pd3aV** transition is associated with the reduction of the Pd centre from Pd^+ to Pd^0.

In summary, carbonate CO_3^{2-} species show coordination patterns different from CO and CO_2 moieties: they tie to the ceria support or metal centres via O atoms, whereas the C atom does not participate in adsorbate–substrate interaction. From the comparison of CO_2 binding energies at the metal-free and M-containing sites, it follows that CO_2 binds slightly more strongly in MCO_3/NP[0/2] structures than in CO_3/NP[0/2]. Conversely, the creation of an extra O vacancy stronger stabilises the formation of the carbonates at metal-free NPs than that at metal-containing NPs.

3.2. Reaction Energies

In this section, we consider the energies of CO to CO_2 oxidation, E^*_{ox}, and of CO_2 to CO_3 transformation, E^*_{CO3}, along with the corresponding activation barriers, $E^{\neq}$, calculated for Pd/NP and Ag/NP models in comparison with the bare NP model. Data in Table 2 show that i) all these reactions are exothermic and ii) activation barriers for the carbonate formation are often higher than for the oxidation of CO.

Bare NPs adsorb CO very weakly, by less than 0.3 eV (Table 1, Figure 2). The extraction of lattice O and the formation of ceria-supported CO_2 yield energies of 0.9–1.4 eV and require 0.8–1.0 eV of activation (Table 2). Because of the low CO_2 desorption barriers,

0.15–0.25 eV (Table 1, $E_{des}(CO_2) = -E_b(CO_2)$ for **2a** and **2aV**), the formed $CO_2/Ce_{21}O_{42}$ and $CO_2/Ce_{21}O_{41}$ complexes can quite easily decompose. Otherwise, they are expected to exothermically transform into carbonates with activation barriers ranging from low—0.27 eV (for CO_2/NP[0/1])—to moderate—0.82 eV (for CO_2/NP[1/1])—values. The thermodynamic stability of such surface carbonate complexes makes them most probable candidates for experimental detection [68].

CO binds very weakly at the defect-free PdO_4 site of the Pd/NP[0/0] complex with an adsorption energy of −0.1 eV (**Pd1b** in Table 1). CO_2 can form via the interaction of the adsorbed CO with a lattice O atom. The process, which is exothermic by 1.3 eV, requires the overcoming of a barrier of 0.5 eV (Table 2). The formed CO_2 molecule is quite strongly bound, with a desorption energy of 1.2 eV (Table 1, $E_{des}(CO_2) = -E_b(CO_2)$ for **Pd2a**). Overcoming an even higher barrier of 1.8 eV (Table 2) is needed to extract one more lattice O centre and activate the transformation of CO_2 to CO_3^{2-}, which is exothermic by only 0.25 eV. CO is strongly, by 1.7 eV, adsorbed at the O-deficient PdO_3 site (**Pd1aV** in Table 1). The formed stable O_3PdCO species can transform to O_2PdCO_2 with an activation barrier of 1.1 eV and moderate reaction exothermicity of 0.6 eV (Table 2). Slightly exothermic by 0.3 eV, the formation of carbonate is hindered by a high energy barrier of 1.8 eV. A much lower energy barrier of 0.7 eV ($-E_b(CO_2)$ for **Pd2aV** in Table 1) is required to desorb the CO_2 molecule into the gas phase. Thus, the most likely ceria-supported Pd-intermediates to be detected in reaction medium are saturated square-planar O_3PdCO/NP (**Pd1aV**) and O_3PdCO_2/NP (**Pd2a**) complexes whose formation proceeds with a sizable energy release (1.3–1.7 eV) and moderate activation barriers of 0.5 eV and whose decomposition is hindered by substantial barriers of about 1.1–1.2 eV.

The reactivity of Ag-containing systems is different (Table 2). CO adsorption on defect-free and O-deficient Ag/NP systems occurs with a moderate energy gain of 0.8 eV (Table 1). The formed O_4AgCO and O_3AgCO species are converted into the corresponding O_3AgCO_2 and O_2AgCO_2 species with a similar exothermicity around 0.4 eV, but the activation barrier for the more O-saturated complex O_4AgCO, 0.9 eV, is 0.4 eV higher than that for O_3AgCO (Table 2). Despite the high exothermicity of 1.2–1.5 eV, the transformation to carbonates is hindered by barriers of ~0.8–1.7 eV. Alternatively, the decomposition with CO_2 desorption should proceed quite readily (see $-E_b(CO_2)$ values for **Ag2b** and **Ag2aV** in Table 1). Thus, the carbonyl complexes O_4AgCO/NP (**Ag1a**) and O_3AgCO (**Ag1aV**), which are easily formed with notable energy gains, are expected to be detectable in a reaction medium. The detection of carboxylate $AgCO_2$/NP (**Ag2b** and **Ag2aV**) complexes seems problematic due to their instability with respect to CO_2 desorption.

We estimated the propensity of CO to CO_2 transformation by the energy of the CO(gas) + M/NP[n/0] → CO_2(gas) + M/NP[n/1] oxidation reaction, E_{ox} (Equations (5) and (6)). It is directly connected with the ease of O release from the ceria lattice and O vacancy creation (Table 2).

Let us compare the oxidation reaction energy E_{ox} calculated for the O_4-site of CeO_2 NP with the calculated energies for clean ceria surfaces [65,71,74,79,80] and the Pd_1–ceria interfaces [8,9,20]. This reaction was found to be slightly, by 0.4–0.6 eV, exothermic on bare CeO_2(111) [74,79] and notably more exothermic on CeO_2(110) [65,74,78,79], at 1.1–1.8 eV. The calculated reaction exothermicity further drastically increases to 3.1 eV for the CeO_2(100) surface with the most exposed O atoms [71]. Our calculated E_{ox} energies for the stoichiometric and O-deficient NP{100} sites, −1.44 and −1.01 eV, respectively (Table 2), are considerably lower than those for the CeO_2(100) surface, but in a similar range to that for CeO_2(110) (assuming that the E_{ox} value should increase by ca. 0.5 eV when the U value is increased from 4 to 5 eV [62]).

At the Pd_1/CeO_2(100) and O_1Pd_1/CeO_2(100) sites, the conversion of CO to CO_2 was characterised by energy yields of 0.6 and 1.2 eV [9], respectively—markedly lower than at the pristine CeO_2(100) surface. The reaction is also moderately exothermic at the Pd_1/CeO_2(110) interface, by 1.2 eV [20], and highly exothermic at the isolated O_1Pd_1 and O_2Pd_1 species on the CeO_2(111) surface, by 2.9 and 2.7 eV [8]—much more exothermic than

at the regular CeO_2(111) surface because of exposing weakly bonded O atoms. Compared to the above-mentioned transformations, that at Pd/NP[0/0] has the lowest E_{ox} of −0.23 eV. There, the formal migration of an O-atom of the O_4Pd moiety to become a part of CO_2 molecule is difficult even in comparison with the three-coordinated O centre of the regular CeO_2(111) surface. For the conversion at the Pd/NP[1/0] site with E_{ox} = −1.61 eV, the relocation of the second O atom of the O_4Pd moiety is more favourable than of the O atom of the isolated O_1Pd_1 moiety on CeO_2(100) or Pd_1 at CeO_2(110), but less beneficial than that of O_1Pd_1 or O_2Pd_1 ad-species on CeO_2(111). For the reactions on Ag/NP[n/0] sites, the energy E_{ox}, −1.0–1.2 eV, is slightly lower than on the Pd/NP[1/0] site, thus approaching E_{ox} values for O_1Pd_1/CeO_2(100) and Pd_1/CeO_2(110) systems. Therefore, our model ceria particle with the Pd atom adsorbed on the O-defective {100} nanofacet appears to be more reactive in CO to CO_2 oxidation than its formal analogue of the Pd-doped extended CeO_2(100) surface.

Thus, the trend for lowering E_{ox} in bare and M-containing ceria systems is Pd/NP[1/0] > NP[n/0] ≈ Ag/NP[n/0] > Pd/NP[0/0], which correlates with the growth of the O vacancy formation energy in the same row (Table 2). Note that the reactivity in CO oxidation of both Ag/NP complexes—with and without an O vacancy near the Ag atom—is similar. Conversely, the presence of an O vacancy in the vicinity of Pd atom is mandatory for CO oxidation at Pd/NP systems to proceed. This makes two consequent steps of CO oxidation at the $Pd/Ce_{21}O_{42}$ nanoparticle problematic. Such characteristics of the studied models as moderately strong CO adsorption, exothermic overall CO oxidation process, sufficiently low barriers of MCO to MCO_2 transformations, and ease of CO_2 desorption render CO oxidation by lattice ceria oxygen atoms more favourable at the sites with Ag than with Pd. Comparing the reaction and activation energies of CO to CO_2 and CO_2 to CO_3 conversions for M-containing ceria NPs, we conclude that the most probable species to be observed experimentally are AgCO and PdCO carbonyls and carboxylate $PdCO_2$ species. Unlike purely ceria nanoparticles, the formation of silver and palladium carbonates is prohibited by high activation barriers. We note, however, that for precise information on the species present in the reaction medium at equilibrium, a microkinetic modelling is required, which is out of the scope of the present study.

3.3. CO_x Vibrational Fingerprints

Several studies reported measured [7,9,16,25,26,28,68,81] and calculated [8,9,68,82–84] vibrational frequencies of CO, CO_2, and CO_3^{2-} groups in the complexes formed by the interaction of CO or CO_2 with cerium-based substrates. The calculated frequencies for selected stretching vibrations of CO_x subsystems of the structures displayed in Figures 2–4 are collected in Table 3.

Our modelling revealed that the CO stretching frequency, ν(CO), for the molecule attached to a cerium ion in M-free systems **1a** and **1aV** and Pd-containing model **Pd1a** shifts by 27–34 cm^{-1} to the short-wave region, which agrees with the measured blue shifts of 27–32 cm^{-1} (vs. 2143 cm^{-1} for free molecule [85]) for CO interacting with the Ce^{4+} centres of the nanostructured CeO_2 [19,86]. Note that the quantitatively precise reproduction of measured vibrational frequencies of CO on ceria requires going beyond the U-corrected generalised-gradient exchange-correlation functionals to hybrid-type functionals [81]. In contrast, ν(CO) for the fragments with M_1-CO bonding formed on M/NP[n/0] substrates shows redshifts of 50–113 cm^{-1}, consistent with the C-O bond elongation by 1–2 pm. Among the models containing Pd_1 species, the **Pd1b** complex with Pd^{2+} cation coordinated by four two-coordinated O anions reveals a medium redshift of 84 cm^{-1}, and the maximum redshifts of 109–113 cm^{-1} are identified for the other two complexes, **Pd1c** and **Pd1aV**, with three-fold coordinated Pd^+ and Pd^{2+} cations (Table 3). For the earlier examined systems with Pd-CO bonds, the redshifts Δν(CO) were calculated to increase from 6 to 96 cm^{-1} in the order O_2Pd_1/CeO_2(111) < O_1Pd_1/CeO_2(100) ≈ O_1Pd_1/CeO_2(111) < Pd_1/CeO_2(100) < Pd_1/CeO_2(111) [8,9]. These values are comparable with those attributed to the CO molecule contacting one Pd atom in experimental studies of Pd/CeO_2, 13–123 cm^{-1} [7,28]

and 10–69 cm^{-1} [9,16,25] and PdO/CeO_2, 58 cm^{-1} [26]. Note that the Δν(CO) redshifts for CO coordinated to the supported Pd cations are opposite to the blue shift for the free $PdCO^+$ ion, measured at 63 cm^{-1} and calculated at 75 cm^{-1} (B3LYP), but approach a redshift for the neutral PdCO molecule, measured at 87 cm^{-1} and calculated at 99 cm^{-1} [70]. The redshifts of ν(CO) for **Ag1a** and **Ag1aV** complexes, at 50 and 61 cm^{-1}, respectively, are smaller than those for the Pd_1-CO moieties and correspond to about one-third of the calculated redshift for the AgCO molecule, 144 cm^{-1} [87]. Similarly large frequency redshifts to those obtained for CO on single Ag and Pd cations on a ceria NP were calculated for CO adsorbed on Pt^+ and Pd^{2+} cations anchored to ceria [83].

Table 3. Calculated vibrational frequencies ν(CO), ν(CO_2) and ν(CO_3) for the systems depicted in Figures 2–4 along with the corresponding frequency shifts Δν(CO) and Δν(CO_2) with respect to calculated vibrational frequencies of free molecules CO (ν(free CO) = 2131 cm^{-1}) and CO_2 (ν_{asym}(free CO_2) = 2363 cm^{-1}).

System [a]	ν(CO) cm^{-1}	Δν(CO) cm^{-1}	ν(CO_2) cm^{-1}	Δν(CO_2) cm^{-1}	ν(CO_3) cm^{-1}
Complexes with CO					
Pd1a	2158	27	-	-	-
Pd1b	2047	−84	-	-	-
Pd1c	2022	−109	-	-	-
Pd1aV	2018	−113	-	-	-
Ag1a	2081	−50	-	-	-
Ag1aV	2070	−61	-	-	-
1a	2162	31	-	-	-
1aV	2165	34	-	-	-
Complexes with CO_2					
Linear O-C-O					
Pd2b	-	-	2323	−40	-
Pd2bV	-	-	2332	−31	-
Ag2a	-	-	2348	−15	-
Ag2bV	-	-	2350	−13	-
2a	-	-	2354	−9	-
2aV	-	-	2360	−3	-
Bent O-C-O					
Pd2a	-	-	1535	−828	-
Pd2aV	-	-	1628	−735	-
Ag2aV	-	-	1332	−1031	-
Ag2b	-	-	1950	−413	-
2bV	-	-	1657	−706	-
Complexes with CO_3^{2-}					
Tridentate					
Pd3a	-	-	-	-	1573; 1221
Pd3b	-	-	-	-	1451; 1243
Pd3aV	-	-	-	-	1442; 1309
Ag3a	-	-	-	-	1511; 1233
Ag3aV	-	-	-	-	1434; 1337
3b	-	-	-	-	1442; 1280
3aV	-	-	-	-	1400; 1353
Bidentate					
Pd3c	-	-	-	-	1746; 1118
Pd3bV	-	-	-	-	1729; 1122
Ag3b	-	-	-	-	1689; 1126
Ag3bV	-	-	-	-	1752; 1169
3a	-	-	-	-	1714; 1082
3bV	-	-	-	-	1704; 1101

[a] For system designations see Figures 2–4.

The highest frequencies of CO_2 stretching vibrations in **2a**, **2aV**, **Ag2a**, **Ag2bV**, **Pd2b**, and **Pd2bV** complexes with a linear CO_2 moiety are close to that of the IR active CO_2 asymmetric stretching frequency of the free molecule; the negative shift $\Delta\nu(CO_2)$ does not exceed 40 cm^{-1} (Table 3). The redshift $\Delta\nu(CO_2)$ for a bent CO_2 fragment in **2bV**, 706 cm^{-1}, is comparable to the experimental value for the free anion CO_2^-, 691 cm^{-1} [88] (vs. measured $\nu(CO_2)$ of free molecule 2349 cm^{-1} [76]) and CO_2^- species at TiO_2 surface, 709 cm^{-1} [89]. The redshift $\Delta\nu(CO_2)$ for the MCO_2/NP[n/1] systems having the M-C bond from 413 to 1031 cm^{-1} is associated with the bending of the CO_2 moiety and C-O bond elongation by 3 to 14 pm. The redshifts for $PdCO_2$/NP systems, 828 cm^{-1} (**Pd2a**) and 735 cm^{-1} (**Pd2aV**), are in the range of values 610–850 cm^{-1} reported for coordination compounds with CO_2 attached to a single d-metal atom [76], while redshift $\Delta\nu(CO_2)$ in **Ag2b** is smaller, at only 413 cm^{-1}. $\Delta\nu(CO_2)$ for the CO_2^{2-} group in **Ag2aV** with CO bonds elongated by 14 pm compared to those of free CO_2 matches the measured redshifts of 1020–1079 cm^{-1} for carbonite ions at CeO_2 [90] and in Cs_2CO_2 [91]. Thus, the increased redshift $\Delta\nu(CO_2)$ seems to correlate with C-O bond elongation, **Ag2b** < **Pd2aV** < **Pd2a** < **Ag2aV** (Table 1).

Differences in the length of the intramolecular C-O bonds are considered among the main factors determining the frequency splitting of CO_3^{2-} stretching vibrations [68]. In tridentate CO_3/NP[n/2] and MCO_3/NP[n/2] complexes, the C-O bond lengths are 125–135 pm for the 1.11- and 1.21-modes, and in less symmetrical bidentate 1.20- and 1.30-structures, the C-O bonds cover a wider interval 121–146 pm.

Overall, the splitting of C-O frequencies is lower for more symmetrical species. In particular, for the two highest frequencies (ν_1 and ν_2), it is only 47 cm^{-1} for 2.2.2-structures, increasing to 97–133 cm^{-1} for 2.2.1-isomers and 162–252 cm^{-1} for 1.2.1- and 1.1.1-isomers (Table 3). For 1.20- and 1.30-carbonates, the splitting becomes as high as 563–632 cm^{-1}. According to earlier calculations, carbonate groups attached to nanostructured ceria surface by three oxygen atoms, represented by sets of 1.21-, 1.2.1- and 1.3.1-structures, are characterised by ν_1 values from 1590 to 1490 cm^{-1} [68]. With the inclusion of ν_1 values for tridentate structures **3b** and **3aV**, this range extends to 1400 cm^{-1}. The calculated ν_1 for tridentate carbonates corresponds to a broad experimental region of 1620–1450 cm^{-1} attributed to the high-frequency vibrations of the carbonate groups formed on surfaces with oxygen vacancies, as well as on facet, edge, and corner sites of ceria particles [68]. The ν_1 frequencies for tridentate carbonate **Ag3a**, **Pd3a**, **Pd3b**, **Ag3aV**, and **Pd3aV** complexes, of 1573–1434 cm^{-1}, fall between the limits of the clean surface of the nanostructured ceria. The ν_1 values for 1.20-carbonate groups in **3a** and **3bV** systems are in a narrow range of 1718–1698 cm^{-1} for bidentate carbonates [68] corresponding to the measured frequency interval of 1732–1722 cm^{-1} [68]. The ν_1 frequencies of the M-containing 1.30-complexes **Pd3c, Pd3bV, Ag3b,** and **Ag3bV** are in a broader range of 1752–1689 cm^{-1}, which includes the interval for bidentate CO_3^{2-} on M-free ceria substrates.

The calculated ν_2 frequency range of the complexes on the clean ceria surface is 1353–1227 cm^{-1}. This corresponds to the experimental frequencies of 1380 and 1280 cm^{-1} [68]. The ν_2 values for tridentate 1.21- and 2.2.1-carbonates **P3b, Pd3aV, Ag3a,** and **Ag3aV** for M-containing systems, at 1340–1220 cm^{-1}, are between these limits, and that for the 1.11-**Pd3a** isomer is only 6 cm^{-1} below the low-end threshold. The ν_2 frequencies are distributed between 1194 and 1082 cm^{-1} for bidentate carbonates depicted in Figure 2 and those examined in [68]; the related experimental values are 1147–1133 cm^{-1} [68].

The range of ν_2 for the CO_3 moieties coordinated in a bidentate way at M/NP systems is 1170–1120 cm^{-1}. Thus, the frequency ranges are similar for the metal-free CO_3/NP and MCO_3/NP sites, making the discrimination between the metal-containing and bare ceria particles solely on the basis of the vibrational spectroscopy data problematic.

In summary, our calculations show that the C-O stretching vibrations of the ceria-supported PdCO and AgCO fragments feature redshifts up to ~110 cm^{-1}, which is at variance with the blue shift at metal-free ceria. Redshifts of CO_2 asymmetric stretching frequency of the M-CO_2 fragments are much higher, up to ~830 cm^{-1} for carboxy-

late MCO_2 and further increasing by ~200 cm^{-1} for carbonite $AgCO_2$. The two highest $\nu(CO_3)$ stretching frequencies of M-CO_3 structures lie in intervals 1755–1690 cm^{-1} and 1170–1120 cm^{-1} for the CO_3 moiety coordinated in a bidentate fashion and 1575–1430 cm^{-1} and 1340–1220 cm^{-1} for the CO_3 in the tridentate coordination.

4. Conclusions

CO_x intermediates formed upon CO adsorption and oxidation on single M = Pd and Ag atoms coordinated to the O_4-site on the {100} facet of a $Ce_{21}O_{42}$ nanoparticle have been studied computationally. Equilibrium structures, CO_x vibrational frequencies, and energetic parameters of various MCO_x-containing complexes have been determined. The influence of the creation of an O vacancy nearby the M atom has been also investigated. The stability of the CO_x moieties anchored to the ceria-supported M atom is found to increase in the order MCO < MCO_2 < MCO_3, similar to the trend for CO_x species adsorbed on M-free ceria NP.

Except for the Pd atom saturated by four O atoms of the ceria surface O_4-site, which is unable to properly adsorb CO, the doping of the ceria nanoparticle with Pd and Ag atom increases its propensity to bind the CO molecule with respect to bare ceria material. In particular, the CO adsorption energy value reaches −1.7 eV for a PdCO unit on a ceria nanoparticle with a nearby O vacancy. CO binding in AgCO complexes, regardless of the presence or absence of a nearby O vacancy, is moderately strong, at −0.8 eV. All these species are the most probable candidates to be detected experimentally, also due to the presence of moderate barriers for CO oxidation (0.5–1.0 eV). In contrast to the blue shift for CO adsorbed on pristine ceria, red shifts of the C-O stretching (vs. free CO) have been calculated for MCO species anchored to ceria. The red shifts of the CO stretching frequency are higher for complexes of Pd and increase with the decreasing coordination of M from MO_4 to MO_3 for a particular metal: $Ag/Ce_{21}O_{42}$ (50 cm^{-1}) < $Ag/Ce_{21}O_{41}$ (61 cm^{-1}) < $Pd/Ce_{21}O_{42}$ (84 cm^{-1}) < $Pd/Ce_{21}O_{41}$ (113 cm^{-1}).

Carboxylate CO_2^- and carbonite CO_2^{2-} (for Ag-doped NP with an O vacancy) complexes featuring a bent CO_2 moiety are formed upon CO oxidation at the M/ceria interface. Contrary to $AgCO_2$-species, which are easily decomposed via CO_2 detachment, $PdCO_2$ moieties are prone to withstand decomposition due to significant CO_2 desorption energies of 0.7–1.2 eV. These $PdCO_2$ moieties anchored to ceria particles could be experimentally detected by the red shifts of the CO_2 asymmetric stretching frequency (vs. that of free CO_2 molecule) by 828 cm^{-1} (one O vacancy nearby Pd) and 735 cm^{-1} (two O vacancies nearby Pd).

Unlike pristine ceria, carbonate structures at ceria-supported Pd and Ag atoms are hardly formed before CO_2 desorption due to the high barriers of CO_2 transformation to CO_3^{2-} (up to 1.8 eV for $PdCO_3$ moieties) and weak CO_2 binding (below ~0.2 eV for $AgCO_3$ moieties). Detailed analysis of the vibrational spectra of MCO_3/NP complexes has shown that the two highest $\nu(CO_3)$ stretching frequencies lie in the well-resolved intervals 1755–1690 and 1170–1120 cm^{-1} for the CO_3 moiety coordinated in a bidentate fashion and 1575–1430 and 1340–1220 cm^{-1} for the carbonate groups in the tridentate coordination. These frequency ranges are similar to those for the M-free CO_3/NP sites. Thus, discrimination between the M-containing and bare ceria particles solely using vibrational spectroscopy data seems hardly possible.

In summary, such characteristics of the studied models as moderately strong CO adsorption, an exothermic CO oxidation process, sufficiently low barriers of MCO to MCO_2 transformations, and ease of CO_2 desorption render CO oxidation by lattice ceria oxygen atoms more favourable at the sites with Ag than with Pd.

Supplementary Materials: The following data are available online at https://www.mdpi.com/article/10.3390/ma14226888/s1: Coordinates of the atomic positions of all considered $Ce_{21}O_{42-\delta}$, $CO_x/Ce_{21}O_{42-\delta}$, $AgCO_x/Ce_{21}O_{42-\delta}$ and $PdCO_x/Ce_{21}O_{42-\delta}$ complexes and selected transition state structures connecting these complexes along with their total energies.

Author Contributions: Conceptualisation, V.A.N., E.A.I.-S. and K.M.N.; methodology, V.A.N. and E.A.I.-S.; software, V.A.N. and S.S.L.; investigation, V.A.N. and S.S.L.; validation, V.A.N. and E.A.I.-S.; formal analysis, V.A.N., A.M.S. and E.A.I.-S.; resources, V.A.N. and E.A.I.-S.; data curation, V.A.N.; writing—original draft preparation, V.A.N., E.A.I.-S. and K.M.N.; writing—review and editing, V.A.N., E.A.I.-S., A.M.S., S.S.L. and K.M.N.; visualisation, V.A.N. and A.M.S.; supervision, V.A.N., E.A.I.-S. and K.M.N. All authors have read and agreed to the published version of the manuscript.

Funding: This work was conducted within the framework of the budget project No. 0287-2021-0012 for Institute of Chemistry and Chemical Technology SB RAS. The work of K.M.N. was funded by the Spanish Government MCIN/AEI/10.13039/501100011033 via grants PGC2018-093863-B-C22, MDM-2017-0767 and PRX17/00348 as well as by the grant 2017SGR13 of the Generalitat de Catalunya.

Institutional Review Board Statement: Not applicable.

Informed Consent Statement: Not applicable.

Data Availability Statement: Data is contained within the article or Supplementary Material.

Acknowledgments: The authors thank the Supercomputer Center of the Institute of Computational Modeling SB RAS for providing computational resources. K.M.N. thanks the European Cooperation in Science and Technology program via the COST Action 18234.

Conflicts of Interest: The authors declare no conflict of interest.

References

1. Grabchenko, M.V.; Mikheeva, N.N.; Mamontov, G.V.; Salaev, M.A.; Liotta, L.F.; Vodyankina, O.V. Ag/CeO_2 Composites for Catalytic Abatement of CO, Soot and VOCs. *Catalysts* **2018**, *8*, 285. [CrossRef]
2. Grabchenko, M.V.; Mamontov, G.V.; Zaikovskii, V.I.; La Parola, V.; Liotta, L.F.; Vodyankina, O.V. The Role of Metal–Support Interaction in Ag/CeO_2 Catalysts for CO and Soot Oxidation. *Appl. Catal. B Environ.* **2020**, *260*, 118148. [CrossRef]
3. Shimizu, K.; Kawachi, H.; Satsuma, A. Study of Active Sites and Mechanism for Soot Oxidation by Silver-Loaded Ceria Catalyst. *Appl. Catal. B* **2010**, *96*, 169–175. [CrossRef]
4. Bera, P.; Patil, K.C.; Hegde, M.S. NO Reduction, CO and Hydrocarbon Oxidation over Combustion Synthesized Ag/CeO_2 Catalyst. *Phys. Chem. Chem. Phys.* **2000**, *2*, 3715–3719. [CrossRef]
5. Tan, H.; Wang, J.; Yu, S.; Zhou, K. Support Morphology-Dependent Catalytic Activity of Pd/CeO_2 for Formaldehyde Oxidation. *Environ. Sci. Technol.* **2015**, *49*, 8675–8682. [CrossRef]
6. Colussi, S.; Gayen, A.; Camellone, M.F.; Boaro, M.; Llorca, J.; Fabris, S.; Trovarelli, A. Nanofaceted Pd-O Sites in Pd-Ce Surface Superstructures: Enhanced Activity in Catalytic Combustion of Methane. *Angew. Chem. Int. Ed.* **2009**, *48*, 8481–8484. [CrossRef] [PubMed]
7. Boronin, A.I.; Slavinskaya, E.M.; Danilova, I.G.; Gulyaev, R.V.; Amosov, Y.u.I.; Kuznetsov, P.A.; Polukhina, I.A.; Koscheev, S.V.; Zaikovskii, V.I.; Noskov, A.S. Investigation of Palladium Interaction with Cerium Oxide and Its State in Catalysts for Low-Temperature CO Oxidation. *Catal. Today* **2009**, *144*, 201–211. [CrossRef]
8. Spezzati, G.; Su, Y.; Hofmann, J.P.; Benavidez, A.D.; DeLaRiva, A.T.; McCabe, J.; Datye, A.K.; Hensen, E.J.M. Atomically Dispersed Pd–O Species on CeO_2(111) as Highly Active Sites for Low-Temperature CO Oxidation. *ACS Catal.* **2017**, *7*, 6887–6891. [CrossRef]
9. Spezzati, G.; Benavidez, A.D.; DeLaRiva, A.T.; Su, Y.; Hofmann, J.P.; Asahina, S.; Olivier, E.J.; Neethling, J.H.; Miller, J.T.; Datye, A.K.; et al. CO Oxidation by Pd Supported on CeO_2(100) and CeO_2(111) Facets. *Appl. Catal. B* **2019**, *243*, 36–46. [CrossRef]
10. Wang, J.; Chen, H.; Hu, Z.; Yao, M.; Li, Y. A Review on the Pd-Based Three-Way Catalyst. *Catal. Rev.* **2015**, *57*, 79–144. [CrossRef]
11. Carraro, F.; Fapohunda, A.; Paganini, M.C.; Agnoli, S. Morphology and Size Effect of Ceria Nanostructures on the Catalytic Performances of Pd/CeO_2 Catalysts for Methanol Decomposition to Syngas. *ACS Appl. Nano Mater.* **2018**, *1*, 1492–1501. [CrossRef]
12. Fan, L.; Fujimoto, K. Reaction Mechanism of Methanol Synthesis from Carbon Dioxide and Hydrogen on Ceria-Supported Palladium Catalysts with SMSI Effect. *J. Catal.* **1997**, *172*, 238–242. [CrossRef]
13. Guo, C.; Wei, S.; Zhou, S.; Zhang, T.; Wang, Z.; Ng, S.-P.; Lu, X.; Wu, C.-M.L.; Guo, W. Initial Reduction of CO_2 on Pd-, Ru-, and Cu-Doped CeO_2(111) Surfaces: Effects of Surface Modification on Catalytic Activity and Selectivity. *ACS Appl. Mater. Interfaces* **2017**, *9*, 26107–26117. [CrossRef]
14. Farmer, J.A.; Campbell, C.T. Ceria Maintains Smaller Metal Catalyst Particles by Strong Metal-Support Bonding. *Science* **2010**, *329*, 933–936. [CrossRef]
15. Lykhach, Y.; Kozlov, S.M.; Skála, T.; Tovt, A.; Stetsovych, V.; Tsud, N.; Dvořák, F.; Johánek, V.; Neitzel, A.; Mysliveček, J.; et al. Counting Electrons on Supported Nanoparticles. *Nat. Mater.* **2016**, *15*, 284–288. [CrossRef]
16. You, R.; Li, Z.; Cao, T.; Nan, B.; Si, R.; Huang, W. Synthesis in a Glovebox: Utilizing Surface Oxygen Vacancies To Enhance the Atomic Dispersion of Palladium on Ceria for Carbon Monoxide Oxidation and Propane Combustion. *ACS Appl. Nano Mater.* **2018**, *1*, 4988–4997. [CrossRef]

17. Boronin, A.I.; Slavinskaya, E.M.; Figueroba, A.; Stadnichenko, A.I.; Kardash, T.Y.; Stonkus, O.A.; Fedorova, E.A.; Muravev, V.V.; Svetlichnyi, V.A.; Bruix, A.; et al. CO Oxidation Activity of Pt/CeO_2 Catalysts Below 0 °C: Platinum Loading Effects. *Appl. Catal. B Environ.* **2021**, *286*, 119931. [CrossRef]
18. Pentyala, P.; Deshpande, P.A. CO Oxidation over $Ce_{1-x}Pd_xO_{2-\delta}$ Takes Place via Vacancy Hopping. *Ind. Eng. Chem. Res.* **2019**, *58*, 7964–7972. [CrossRef]
19. Wu, Z.; Li, M.; Overbury, S.H. On the Structure Dependence of CO Oxidation over CeO_2 nanocrystals with well-defined surface planes. *J. Catal.* **2012**, *285*, 61–73. [CrossRef]
20. Song, W.; Su, Y.; Hensen, E.J.M. A DFT Study of CO Oxidation at the Pd–CeO_2(110) Interface. *J. Phys. Chem. C* **2015**, *119*, 27505–27511. [CrossRef]
21. Groppi, G.; Cristiani, C.; Lietti, L.; Ramella, C.; Valentini, M.; Forzatti, P. Effect of Ceria on Palladium Supported Catalysts for High Temperature Combustion of CH_4 under Lean Conditions. *Catal. Today* **1999**, *50*, 399–412. [CrossRef]
22. Sharma, S.; Hilaire, S.; Vohs, J.M.; Gorte, R.J.; Jen, H.-W. Evidence for Oxidation of Ceria by CO_2. *J. Catal.* **2000**, *190*, 199–204. [CrossRef]
23. Scanlon, D.O.; Morgan, B.J.; Watson, G.W. The Origin of the Enhanced Oxygen Storage Capacity of $Ce_{1-x}(Pd/Pt)_xO_2$. *Phys. Chem. Chem. Phys.* **2011**, *13*, 4279. [CrossRef]
24. Chang, S.; Li, M.; Hua, Q.; Zhang, L.; Ma, Y.; Ye, B.; Huang, W. Shape-Dependent Interplay between Oxygen Vacancies and Ag–CeO_2 Interaction in Ag/CeO_2 Catalysts and Their Influence on the Catalytic Activity. *J. Catal.* **2012**, *293*, 195–204. [CrossRef]
25. Hu, Z.; Liu, X.; Meng, D.; Guo, Y.; Guo, Y.; Lu, G. Effect of Ceria Crystal Plane on the Physicochemical and Catalytic Properties of Pd/Ceria for CO and Propane Oxidation. *ACS Catal.* **2016**, *6*, 2265–2279. [CrossRef]
26. Meng, L.; Jia, A.-P.; Lu, J.-Q.; Luo, L.-F.; Huang, W.-X.; Luo, M.-F. Synergetic Effects of PdO Species on CO Oxidation over PdO–CeO_2 Catalysts. *J. Phys. Chem. C* **2011**, *115*, 19789–19796. [CrossRef]
27. Gulyaev, R.V.; Kardash, T.Y.; Malykhin, S.E.; Stonkus, O.A.; Ivanova, A.S.; Boronin, A.I. The Local Structure of $Pd_xCe_{1-x}O_{2-x-\delta}$ Solid Solutions. *Phys. Chem. Chem. Phys.* **2014**, *16*, 13523–13539. [CrossRef]
28. Craciun, R.; Daniell, W.; Knözinger, H. The Effect of CeO_2 Structure on the Activity of Supported Pd Catalysts Used for Methane Steam Reforming. *Appl. Catal. A* **2002**, *230*, 153–168. [CrossRef]
29. Luches, P.; Pagliuca, F.; Valeri, S.; Illas, F.; Preda, G.; Pacchioni, G. Nature of Ag Islands and Nanoparticles on the CeO_2(111) Surface. *J. Phys. Chem. C* **2012**, *116*, 1122–1132. [CrossRef]
30. Liu, J.-X.; Su, Y.; Filot, I.A.W.; Hensen, E.J.M. A Linear Scaling Relation for CO Oxidation on CeO_2-Supported Pd. *J. Am. Chem. Soc.* **2018**, *140*, 4580–4587. [CrossRef]
31. Shen, M.; Wei, G.; Yang, H.; Wang, J.; Wang, X. Different Selections of Active Sites for CO, C_3H_6, and $C_{10}H_{22}$ Oxidation on Pd/CeO_2 Catalysts. *Fuel* **2013**, *103*, 869–875. [CrossRef]
32. Hiley, C.I.; Fisher, J.M.; Thompsett, D.; Kashtiban, R.J.; Sloan, J.; Walton, R.I. Incorporation of Square-Planar Pd^{2+} in Fluorite CeO_2: Hydrothermal Preparation, Local Structure, Redox Properties and Stability. *J. Mater. Chem. A* **2015**, *3*, 13072–13079. [CrossRef]
33. Su, Y.-Q.; Filot, I.A.W.; Liu, J.-X.; Hensen, E.J.M. Stable Pd-Doped Ceria Structures for CH_4 Activation and CO Oxidation. *ACS Catal.* **2018**, *8*, 75–80. [CrossRef]
34. Priolkar, K.R.; Bera, P.; Sarode, P.R.; Hegde, M.S.; Emura, S.; Kumashiro, R.; Lalla, N.P. Formation of $Ce_{1-x}Pd_xO_{2-\delta}$ Solid Solution in Combustion-Synthesized Pd/CeO_2 Catalyst: XRD, XPS, and EXAFS Investigation. *Chem. Mat.* **2002**, *14*, 2120–2128. [CrossRef]
35. Figueroba, A.; Bruix, A.; Kovács, G.; Neyman, K.M. Metal-Doped Ceria Nanoparticles: Stability and Redox Processes. *Phys. Chem. Chem. Phys.* **2017**, *19*, 21729–21738. [CrossRef]
36. Neitzel, A.; Figueroba, A.; Lykhach, Y.; Skála, T.; Vorokhta, M.; Tsud, N.; Mehl, S.; Ševčíková, K.; Prince, K.C.; Neyman, K.M.; et al. Atomically Dispersed Pd, Ni, and Pt Species in Ceria-Based Catalysts: Principal Differences in Stability and Reactivity. *J. Phys. Chem. C* **2016**, *120*, 9852–9862. [CrossRef]
37. Figueroba, A.; Kovács, G.; Bruix, A.; Neyman, K.M. Towards Stable Single-Atom Catalysts: Strong Binding of Atomically Dispersed Transition Metals on the Surface of Nanostructured Ceria. *Catal. Sci. Technol.* **2016**, *6*, 6806–6813. [CrossRef]
38. Nasluzov, V.A.; Ivanova-Shor, E.A.; Shor, A.M.; Neyman, K.M. Silver Atom, Trimer and Tetramer Species Supported on a Ceria Nanoparticle: A Density Functional Study. *Surf. Sci.* **2019**, *681*, 38–46. [CrossRef]
39. Li, L.; Chang, X.; Lin, X.; Zhao, Z.-J.; Gong, J. Theoretical Insights into Single-Atom Catalysts. *Chem. Soc. Rev.* **2020**, *49*, 8156–8178. [CrossRef]
40. Ding, W.-C.; Gu, X.-K.; Su, H.-Y.; Li, W.-X. Single Pd Atom Embedded in CeO_2(111) for NO Reduction with CO: A First-Principles Study. *J. Phys. Chem. C* **2014**, *118*, 12216–12223. [CrossRef]
41. Nasluzov, V.A.; Neyman, K.M.; Shor, A.M.; Laletina, S.S.; Ivanova-Shor, E.A. Density Functional Calculation of Dioxygen Adsorption at Complexes of Ceria Nanoparticle with Atoms, Trimers and Tetramers of Silver. *J. Sib. Fed. Univ. Chem.* **2016**, *3*, 281–295. [CrossRef]
42. Preda, G.; Pacchioni, G. Formation of oxygen active species in Ag-modified CeO_2 catalyst for soot oxidation: A DFT study, Catal. *Today* **2011**, *177*, 31–38. [CrossRef]
43. Brugnoli, L.; Pedone, A.; Menziani, M.C.; Adamo, C.; Labat, F. O_2 Activation over Ag-Decorated CeO_2 (111) and TiO_2 (110) Surfaces: A Theoretical Comparative Investigation. *J. Phys. Chem. C* **2020**, *124*, 25917–25930. [CrossRef]
44. Bromley, S.T.; de Moreira I, P.R.; Neyman, K.M.; Illas, F. Approaching Nanoscale Oxides: Models and Theoretical Methods. *Chem. Soc. Rev.* **2009**, *38*, 2657. [CrossRef] [PubMed]

45. Bruix, A.; Neyman, K.M. Modeling Ceria-Based Nanomaterials for Catalysis and Related Applications. *Catal. Lett.* **2016**, *146*, 2053–2080. [CrossRef]
46. Loschen, C.; Migani, A.; Bromley, S.T.; Illas, F.; Neyman, K.M. Density Functional Studies of Model Cerium Oxide Nanoparticles. *Phys. Chem. Chem. Phys.* **2008**, *10*, 5730–5738. [CrossRef]
47. Migani, A.; Vayssilov, G.N.; Bromley, S.T.; Illas, F.; Neyman, K.M. Greatly Facilitated Oxygen Vacancy Formation in Ceria Nanocrystallites. *Chem. Comm.* **2010**, *46*, 5936. [CrossRef]
48. Bruix, A.; Neyman, K.M. How to design models for ceria nanoparticles: Challenges and strategies for describing nanostructured reducible oxides. In *Computational Modelling of Nanoparticles, Frontiers of Nanoscience*; Bromley, S.T., Woodley, S.M., Eds.; Elsevier: Oxford, UK, 2018; Volume 12, pp. 55–99, ISBN 978-0-08-102232-0.
49. Bruix, A.; Lykhach, Y.; Matolínová, I.; Neitzel, A.; Skála, T.; Tsud, N.; Vorokhta, M.; Stetsovych, V.; Ševčíková, K.; Mysliveček, J.; et al. Maximum Noble-Metal Efficiency in Catalytic Materials: Atomically Dispersed Surface Platinum. *Angew. Chem. Int. Ed.* **2014**, *53*, 10525–10530. [CrossRef]
50. Aleksandrov, H.A.; Neyman, K.M.; Vayssilov, G.N. The Structure and Stability of Reduced and Oxidized Mononuclear Platinum Species on Nanostructured Ceria from Density Functional Modeling. *Phys. Chem. Chem. Phys.* **2015**, *17*, 14551–14560. [CrossRef]
51. Koleva, I.Z.; Aleksandrov, H.A.; Vayssilov, G.N. Decomposition Behavior of Platinum Clusters Supported on Ceria and γ-Alumina in the Presence of Carbon Monoxide. *Catal. Sci. Technol.* **2017**, *7*, 734–742. [CrossRef]
52. Kresse, G.; Hafner, J. Ab Initio Molecular Dynamics for Liquid Metals. *Phys. Rev. B* **1993**, *47*, 558–561. [CrossRef]
53. Kresse, G.; Furthmüller, J. Efficient Iterative Schemes for Ab Initio Total-Energy Calculations Using a Plane-Wave Basis Set. *Phys. Rev. B* **1996**, *54*, 11169–11186. [CrossRef] [PubMed]
54. Blöchl, P.E. Projector Augmented-Wave Method. *Phys. Rev. B* **1994**, *50*, 17953–17979. [CrossRef] [PubMed]
55. Kresse, G.; Joubert, D. From Ultrasoft Pseudopotentials to the Projector Augmented-Wave Method. *Phys. Rev. B* **1999**, *59*, 1758–1775. [CrossRef]
56. Viñes, F.; Illas, F.; Neyman, K.M. On the Mechanism of Formation of Metal Nanowires by Self-Assembly. *Angew. Chem. Int. Ed.* **2007**, *46*, 7094–7097. [CrossRef] [PubMed]
57. Sk, M.A.; Kozlov, S.M.; Lim, K.H.; Migani, A.; Neyman, K.M. Oxygen Vacancies in Self-Assemblies of Ceria Nanoparticles. *J. Mater. Chem. A* **2014**, *2*, 18329–18338. [CrossRef]
58. Perdew, J.P.; Chevary, J.A.; Vosko, S.H.; Jackson, K.A.; Pederson, M.R.; Singh, D.J.; Fiolhais, C. Atoms, Molecules, Solids, and Surfaces: Applications of the Generalized Gradient Approximation for Exchange and Correlation. *Phys. Rev. B* **1992**, *46*, 6671–6687, Erratum in **1993**, *48*, 4978–4978. [CrossRef]
59. Rohrbach, A.; Hafner, J.; Kresse, G. Electronic Correlation Effects in Transition-Metal Sulfides. *J. Phys. Condens. Matter* **2003**, *15*, 979–996. [CrossRef]
60. Dudarev, S.L.; Savrasov, S.Y.; Humphreys, C.J.; Sutton, A.P. Electron-Energy-Loss Spectra and the Structural Stability of Nickel Oxide: An LSDA+U Study. *Phys. Rev. B* **1998**, *57*, 1505–1509. [CrossRef]
61. Loschen, C.; Carrasco, J.; Neyman, K.; Illas, F. First-Principles LDA+U and GGA+U Study of Cerium Oxides: Dependence on the Effective U Parameter. *Phys. Rev. B* **2007**, *75*, 035117. [CrossRef]
62. Bennett, L.J.; Jones, G. The Influence of the Hubbard U Parameter in Simulating the Catalytic Behaviour of Cerium Oxide. *Phys. Chem. Chem. Phys.* **2014**, *16*, 21032–21038. [CrossRef]
63. Vayssilov, G.N.; Migani, A.; Neyman, K. Density Functional Modeling of the Interactions of Platinum Clusters with CeO_2 Nanoparticles of Different Size. *J. Phys. Chem. C* **2011**, *115*, 16081–16086. [CrossRef]
64. Bruix, A.; Migani, A.; Vayssilov, G.N.; Neyman, K.M.; Libuda, J.; Illas, F. Effects of Deposited Pt Particles on the Reducibility of CeO_2(111). *Phys. Chem. Chem. Phys.* **2011**, *13*, 11384. [CrossRef] [PubMed]
65. Huang, M.; Fabris, S. CO Adsorption and Oxidation on Ceria Surfaces from DFT+U Calculations. *J. Phys. Chem. C* **2008**, *112*, 8643–8648. [CrossRef]
66. Weinan, E.; Ren, W.; Vanden-Eijnden, E. String Method for the Study of Rare Events. *Phys. Rev. B* **2002**, *66*, 052301. [CrossRef]
67. Chaffey-Millar, H.; Nikodem, A.; Matveev, A.V.; Krüger, S.; Rösch, N. Improving Upon String Methods for Transition State Discovery. *J. Chem. Theor. Comput.* **2012**, *8*, 777–786. [CrossRef] [PubMed]
68. Vayssilov, G.N.; Mihaylov, M.; Petkov, P.S.; Hadjiivanov, K.I.; Neyman, K.M. Reassignment of the Vibrational Spectra of Carbonates, Formates, and Related Surface Species on Ceria: A Combined Density Functional and Infrared Spectroscopy Investigation. *J. Phys. Chem. C* **2011**, *115*, 23435–23454. [CrossRef]
69. Hulva, J.; Meier, M.; Bliem, R.; Jakub, Z.; Kraushofer, F.; Schmid, M.; Diebold, U.; Franchini, C.; Parkinson, G.S. Unraveling CO Adsorption on Model Single-atom Catalysts. *Science* **2021**, *371*, 375–379. [CrossRef]
70. Liang, B.; Zhou, M.; Andrews, L. Reactions of Laser-Ablated Ni, Pd, and Pt Atoms with Carbon Monoxide: Matrix Infra-red Spectra and Density Functional Calculations on $M(CO)_n$ (n = 1−4), $M(CO)_n^-$ (n = 1−3), and $M(CO)_n^+$ (n = 1−2), (M = Ni, Pd, Pt). *J. Phys. Chem. A* **2000**, *104*, 3905–3914. [CrossRef]
71. Zhong, S.-H.; Lu, G.; Gong, X.-Q. A DFT+U Study of the Structures and Reactivities of Polar CeO_2(100) Surfaces. *Chinese J. Catal.* **2017**, *38*, 1138–1147. [CrossRef]
72. Kumari, N.; Haider, M.A.; Agarwal, M.; Sinha, N.; Basu, S. Role of Reduced CeO_2(110) Surface for CO_2 Reduction to CO and Methanol. *J. Phys. Chem. C* **2016**, *120*, 16626–16635. [CrossRef]

73. Hahn, K.R.; Iannuzzi, M.; Seitsonen, A.P.; Hutter, J. Coverage Effect of the CO_2 Adsorption Mechanisms on CeO_2(111) by First Principles Analysis. *J. Phys. Chem. C* **2013**, *117*, 1701–1711. [CrossRef]
74. Chen, F.; Liu, D.; Zhang, J.; Hu, P.; Gong, X.-Q.; Lu, G. A DFT+U Study of the Lattice Oxygen Reactivity toward Direct CO Oxidation on the CeO_2(111) and (110) Surfaces. *Phys. Chem. Chem. Phys.* **2012**, *14*, 16573. [CrossRef] [PubMed]
75. Cheng, Z.; Sherman, B.J.; Lo, C.S. Carbon Dioxide Activation and Dissociation on Ceria (110): A Density Functional Theory Study. *J. Chem. Phys.* **2013**, *138*, 014702. [CrossRef] [PubMed]
76. Lu, X.; Wang, W.; Wei, S.; Guo, C.; Shao, Y.; Zhang, M.; Deng, Z.; Zhu, H.; Guo, W. Initial Reduction of CO_2 on Perfect and O-Defective CeO_2(111) Surfaces: Towards CO or COOH? *RSC Adv.* **2015**, *5*, 97528–97535. [CrossRef]
77. Gibson, D.H. Carbon Dioxide Coordination Chemistry: Metal Complexes and Surface-Bound Species. What Relationships? *Coord. Chem. Rev.* **1999**, *185–186*, 335–355. [CrossRef]
78. Albrecht, P.M.; Jiang, D.; Mullins, D.R. CO_2 Adsorption As a Flat-Lying, Tridentate Carbonate on CeO_2(100). *J. Phys. Chem. C* **2014**, *118*, 9042–9050. [CrossRef]
79. Scanlon, D.O.; Galea, N.M.; Morgan, B.J.; Watson, G.W. Reactivity on the (110) Surface of Ceria: A GGA+U Study of Surface Reduction and the Adsorption of CO and NO_2. *J. Phys. Chem. C* **2009**, *113*, 11095–11103. [CrossRef]
80. Nolan, M.; Parker, S.C.; Watson, G.W. CeO_2 Catalysed Conversion of CO, NO_2 and NO from First Principles Energetics. *Phys. Chem. Chem. Phys.* **2006**, *8*, 216. [CrossRef]
81. Binet, C.; Daturi, M.; Lavalley, J.-C. IR Study of Polycrystalline Ceria Properties in Oxidised and Reduced States. *Catal. Today* **1999**, *50*, 207–225. [CrossRef]
82. Lustemberg, P.G.; Plessow, P.N.; Wang, Y.; Yang, C.; Nefedov, A.; Studt, F.; Wöll, C.; Ganduglia-Pirovano, M.V. Vibra-tional Frequencies of Cerium-Oxide-Bound CO: A Challenge for Conventional DFT Methods. *Phys. Rev. Lett.* **2020**, *125*, 256101. [CrossRef] [PubMed]
83. Nolan, M.; Parker, S.C.; Watson, G.W. Vibrational Properties of CO on Ceria Surfaces. *Surf. Sci.* **2006**, *600*, 175–178. [CrossRef]
84. Aleksandrov, H.A.; Neyman, K.M.; Hadjiivanov, K.I.; Vayssilov, G.N. Can the State of Pla¬tinum Species Be Unambiguously Determined by the Stretching Frequency of an Adsorbed CO Probe Molecule? *Phys. Chem. Chem. Phys.* **2016**, *18*, 22108–22121. [CrossRef] [PubMed]
85. Li, C.; Sakata, Y.; Arai, T.; Domen, K.; Maruya, K.; Onishi, T. Carbon Monoxide and Carbon Dioxide Adsorption on Cerium Oxide Studied by Fourier-Transform Infrared Spectroscopy. Part 1.-Formation of Carbonate Species on Dehydroxylated CeO_2, at Room Temperature. *J. Chem. Soc. Faraday Trans.* **1989**, *85*, 929. [CrossRef]
86. Chen, S.; Cao, T.; Gao, Y.; Li, D.; Xiong, F.; Huang, W. Probing Surface Structures of CeO_2, TiO_2, and Cu_2O Nanocrystals with CO and CO_2 Chemisorption. *J. Phys. Chem. C* **2016**, *120*, 21472–21485. [CrossRef]
87. Liang, B.; Andrews, L. Reactions of Laser-Ablated Ag and Au Atoms with Carbon Monoxide: Matrix Infrared Spectra and Density Functional Calculations on $Ag(CO)_n$ (n = 2, 3), $Au(CO)_n$ (n = 1, 2) and $M(CO)_n^+$ (n = 1−4; M = Ag, Au). *J. Phys. Chem. A* **2000**, *104*, 9156–9164. [CrossRef]
88. Jacox, M.E.; Thompson, W.E. The Vibrational Spectra of Molecular Ions Isolated in Solid Neon. I. CO_2^+ and CO_2^-. *J. Chem. Phys.* **1989**, *91*, 1410–1416. [CrossRef]
89. Rasko, J.; Solymosi, F. Infrared Spectroscopic Study of the Photoinduced Activation of CO_2 on TiO_2 and Rh/TiO_2 Catalysts. *J. Phys. Chem.* **1994**, *98*, 7147–7152. [CrossRef]
90. Binet, C.; Badri, A.; Boutonnet-Kizling, M.; Lavalley, J.-C. FTIR Study of Carbon Monoxide Adsorption on Ceria: CO_2^{2-} Carbonite Dianion Adsorbed Species. *J. Chem. Soc. Faraday Trans.* **1994**, *90*, 1023. [CrossRef]
91. Kafafi, Z.H.; Hauge, R.H.; Billups, W.E.; Margrave, J.L. Carbon Dioxide Activation by Alkali Metals. 2. Infrared Spectra of $M^+CO_2^-$ and $M_2^{2+}CO_2^{2-}$ in Argon and Nitrogen Matrixes. *Inorg. Chem.* **1984**, *23*, 177–183. [CrossRef]